

CFHTLenS: The relation between galaxy dark matter haloes and baryons from weak gravitational lensing

Malin Velander^{1,2*}, Edo van Uitert^{1,3}, Henk Hoekstra^{1,4}, Jean Coupon⁵, Thomas Erben³, Catherine Heymans⁶, Hendrik Hildebrandt^{7,3}, Thomas D. Kitching⁶, Yannick Mellier^{8,9}, Lance Miller², Ludovic Van Waerbeke⁷, Christopher Bonnett¹⁰, Liping Fu¹¹, Stefania Giodini¹, Michael J. Hudson^{12,13}, Konrad Kuijken¹, Barnaby Rowe^{14,15}, Tim Schrabback^{1,16,3}, Elisabetta Semboloni¹

¹*Leiden Observatory, Leiden University, Niels Bohrweg 2, 2333 CA Leiden, The Netherlands*

²*Department of Physics, Oxford University, Keble Road, Oxford OX1 3RH, UK*

³*Argelander Institute for Astronomy, University of Bonn, Auf dem Hügel 71, 53121 Bonn, Germany*

⁴*Department of Physics and Astronomy, University of Victoria, Victoria, BC V8P 5C2, Canada*

⁵*Institute of Astronomy and Astrophysics, Academia Sinica, P.O. Box 23-141, Taipei 10617, Taiwan*

⁶*Scottish Universities Physics Alliance, Institute for Astronomy, University of Edinburgh, Royal Observatory, Blackford Hill, Edinburgh, EH9 3HJ, UK*

⁷*University of British Columbia, Department of Physics and Astronomy, 6224 Agricultural Road, Vancouver, B.C. V6T 1Z1, Canada*

⁸*Institut d'Astrophysique de Paris, Université Pierre et Marie Curie - Paris 6, 98 bis Boulevard Arago, F-75014 Paris, France*

⁹*Institut d'Astrophysique de Paris, CNRS, UMR 7095, 98 bis Boulevard Arago, F-75014 Paris, France*

¹⁰*Institut de Ciències de l'Espai, CSIC/IEEC, F. de Ciències, Torre C5 par-2, Barcelona 08193, Spain*

¹¹*Key Lab for Astrophysics, Shanghai Normal University, 100 Guilin Road, 200234, Shanghai, China*

¹²*Dept. of Physics and Astronomy, University of Waterloo, Waterloo, ON, N2L 3G1, Canada*

¹³*Perimeter Institute for Theoretical Physics, 31 Caroline Street N, Waterloo, ON, N2L 1Y5, Canada*

¹⁴*Department of Physics and Astronomy, University College London, Gower Street, London WC1E 6BT, U.K*

¹⁵*California Institute of Technology, 1200 E California Boulevard, Pasadena CA 91125, USA*

¹⁶*Kavli Institute for Particle Astrophysics and Cosmology, Stanford University, 382 Via Pueblo Mall, Stanford, CA 94305-4060, USA*

ABSTRACT

We present a study of the relation between dark matter halo mass and the baryonic content of their host galaxies, quantified through galaxy luminosity and stellar mass. Our investigation uses 154 deg² of Canada-France-Hawaii Telescope Lensing Survey (CFHTLenS) lensing and photometric data, obtained from the CFHT Legacy Survey. To interpret the weak lensing signal around our galaxies we employ a galaxy-galaxy lensing halo model which allows us to constrain the halo mass and the satellite fraction. Our analysis is limited to lenses at redshifts between 0.2 and 0.4, split into a red and a blue sample. We express the relationship between dark matter halo mass and baryonic observable as a power law with pivot points of $10^{11} h_{70}^{-2} L_{\odot}$ and $2 \times 10^{11} h_{70}^{-2} M_{\odot}$ for luminosity and stellar mass respectively. For the luminosity-halo mass relation we find a slope of $1.56^{+0.04}_{-0.06}$ and a normalisation of $1.26^{+0.07}_{-0.06} \times 10^{13} h_{70}^{-1} M_{\odot}$ for red galaxies, while for blue galaxies the best-fit slope is $0.73^{+0.09}_{-0.08}$ and the normalisation is $0.16 \pm 0.03 \times 10^{13} h_{70}^{-1} M_{\odot}$. Similarly, we find a best-fit slope of $1.49^{+0.06}_{-0.04}$ and a normalisation of $1.30^{+0.05}_{-0.09} \times 10^{13} h_{70}^{-1} M_{\odot}$ for the stellar mass-halo mass relation of red galaxies, while for blue galaxies the corresponding values are $0.83^{+0.05}_{-0.04}$ and $0.88 \pm 0.13 \times 10^{13} h_{70}^{-1} M_{\odot}$. All numbers convey the 68% confidence limit. For red lenses, the fraction which are satellites inside a larger halo tends to decrease with luminosity and stellar mass, with the sample being purely satellites for a stellar mass of $2 \times 10^9 h_{70}^{-2} M_{\odot}$. The satellite fractions are generally close to zero for blue lenses, irrespective of luminosity or stellar mass. This, together with the shallower relation between halo mass and baryonic tracer, is a direct confirmation from galaxy-galaxy lensing that blue galaxies reside in less clustered environments than red galaxies. We also find that the halo model, while matching the lensing signal around red lenses well, is prone to over-predicting the large-scale signal for faint and less massive blue lenses. This could be a further indication that these galaxies tend to be more isolated than assumed.

Key words: cosmology: observations – gravitational lensing: weak – galaxies: haloes – dark matter

* E-mail: Malin.Velander@astro.ox.ac.uk

1 INTRODUCTION

In order to fully understand the mechanisms behind galaxy formation, the connection between galaxies and the extensive dark matter haloes in which they are enveloped must be studied in exhaustive detail. In pursuit of this precision, reliable mass estimates of both the baryonic and the dark matter content of galaxies are required. The visible component may be evaluated using galaxy properties such as the luminosity or the stellar mass, properties which can be derived via stellar synthesis models (Kauffmann et al. 2003; Gallazzi et al. 2005; Bell & de Jong 2001; Salim et al. 2007). The dark matter, on the other hand, cannot be observed directly but must be examined through its gravitational influence on the surroundings. At the largest scales reached by haloes, optical tracers such as satellite galaxies are scarce. Furthermore, estimates of halo mass from satellite galaxy kinematics (see, for example, More et al. 2011) do not only require spectroscopic measurements of a very large number of objects, which are unfeasible with current instrumentation, but they also require the application of the virial theorem with all its associated assumptions. To study any and all galaxies it is therefore desirable to use probes independent of these tracers, and independent of the physical state of the halo, but with the power to explore a large range of scales. These requirements are all satisfied by weak gravitational lensing.

Gravitational lensing is a fundamental consequence of gravity. As light from distant objects travels through the Universe it is deflected by intervening matter. This deflection causes the distant objects, or sources, to appear distorted (and magnified). In the weak regime the distortion is minute, and only by studying the shapes of a large number of sources can information about the foreground gravitational field be extracted. By examining the average lensing distortion as a function of distance from foreground galaxies, or lenses, the density profiles of their dark matter haloes may be directly investigated; this technique is known as galaxy-galaxy lensing. First detected by Brainerd et al. (1996), the field of galaxy-galaxy lensing has been growing rapidly, with increasing precision as survey area grows. Our understanding of the underlying physics also increases as the interpretation of the signal becomes more sophisticated. Simulations predict that dark matter haloes are well approximated by Navarro-Frenk-White profiles (NFW; Navarro, Frenk, & White 1996) and comparing such a profile to the observed signal around isolated lenses results in halo mass estimates. Galaxies and their haloes are not generally isolated, however, but reside in clustered environments. The ramification is that the interpretation of the observed galaxy-galaxy lensing signal around foreground lenses becomes more complicated since the signal from neighbouring haloes also influences the result. To address this problem a number of approaches have been employed. Early studies modelled the lensing signal by associating all matter with galaxies and comparing the resulting shear field to the observations in a maximum-likelihood approach (Schneider & Rix 1997; Hudson et al. 1998; Hoekstra et al. 2004). In this case the clustering of galaxies was accounted for through the observed positions and Hudson et al. (1998) explicitly attempted to correct for the offset signal seen by satellite galaxies in larger haloes. It was, however, an approximate description. Alternatively the issue can be circumvented by selecting only isolated lenses (see Hoekstra et al. 2005). This inevitably leads to a large reduction in the number of lenses, and the sample is no longer representative as it does not probe the full range of environments.

Over the past decade a new approach has gained traction: the weak lensing halo model (Cooray & Sheth 2002;

Guzik & Seljak 2002; Mandelbaum et al. 2005b; van Uitert et al. 2011; Leauthaud et al. 2011). Within the halo model framework, all haloes are represented as distinct entities, each with a galaxy at the centre. Enclosed in each main halo are satellite galaxies surrounded by subhaloes. In this work we seek to employ the halo model to gain a more accurate picture of galaxy-size dark matter haloes, allowing for a more precise analysis of the link between galaxies and the dark matter haloes they reside in. For this purpose we use image data from the completed Canada-France-Hawaii Telescope Legacy Survey (CFHTLS), and weak lensing and photometric redshift catalogues produced by the Canada-France-Hawaii Telescope Lensing Survey (CFHTLenS¹; Heymans et al. 2012; Miller et al. 2013; Hildebrandt et al. 2012). This work improves on the preliminary galaxy-galaxy lensing analysis carried out using a small subset of the CFHTLS and a single-halo model fit to the inner regions only (Parker et al. 2007). Furthermore, unlike Coupon et al. (2012) who studied the clustering signal of galaxies for the full CFHTLS-Wide to constrain the evolution in redshift of the stellar-to-halo mass relation, our analysis is based on galaxy-galaxy lensing, which can directly constrain the average halo mass of galaxies on small scales.

Three recent studies to use the galaxy-galaxy lensing halo model to constrain these relations are Mandelbaum et al. (2006), van Uitert et al. (2011) (hereafter VU11) and Leauthaud et al. (2012). Mandelbaum et al. (2006) studied the halo masses of lenses from the full area of the fourth data release of the Sloan Digital Sky Survey (SDSS DR4; Adelman-McCarthy et al. 2006) using a galaxy-galaxy lensing halo model. The SDSS is very wide, but also very shallow which means that for low luminosity galaxies it is highly powerful while it lacks the depth to constrain the halo masses of higher-luminosity galaxies which are at higher redshifts on average. A similar study was performed by VU11 using an earlier implementation of the halo model software used for this paper. That study exploited a 300 deg² overlap between the SDSS DR7 and the intermediate-depth second Red-sequence Cluster Survey (RCS2; Gilbank et al. 2011). The SDSS data were used to identify the lenses, but the lensing analysis was performed on the RCS2, improving greatly at the high mass end on the previous analysis based on the shallow SDSS alone. However, while the VU11 lenses had accurate spectroscopic redshift estimates, there were no redshift estimates available for the sources at the time. Thus the work presented here has, aside from the increased depth down to $z'_{AB} = 24.7$, a further advantage over the VU11 analysis owing to the high-precision photometric redshifts available for all objects used in our analysis (see Hildebrandt et al. 2012). This makes it possible to cleanly separate lenses from sources and therefore minimises the contamination by satellites. It also allows for optimal weighting of the lensing signal.

Leauthaud et al. (2012) combined several techniques to constrain the relation between halo mass and stellar mass using data from the deep space-based Cosmic Evolution Survey (COSMOS; Scoville et al. 2007). They did not, however, refine their results by splitting their lens sample according to galaxy type. In a follow-up paper, Tinker et al. (2012) did split the COSMOS sample into star forming and passive galaxies to study the redshift evolution of the same relation, but limited their study to massive galaxies located centrally in a group-sized halo. Thanks to the large area and depth of the CFHTLenS, we are in this paper able to investigate the relation for blue and red galaxies separately without limiting our sample in that way. We provide here a detailed comparison between

¹ www.cfhtlens.org

our results and those quoted in Mandelbaum et al. (2006), VU11 and Leauthaud et al. (2012), but leave Tinker et al. (2012) due to the large difference in sample selection between our analysis and theirs.

This paper is organised as follows: we introduce the data in Section 2, and in Section 3 we review our halo model and the formalism behind it. We investigate the lensing signal as a function of luminosity in Section 4 and as a function of stellar mass in Section 5. In Section 6 we compare our results to the three previous studies introduced above, and we conclude in Section 7. The following cosmology is assumed throughout (WMAP7; Komatsu et al. 2011): $(\Omega_M, \Omega_\Lambda, h, \sigma_8, w) = (0.27, 0.73, 0.70, 0.81, -1)$.

2 DATA

In this paper we present a galaxy-galaxy weak lensing analysis of the entire Wide part of the Canada-France-Hawaii Telescope Legacy Survey (CFHTLS-Wide). The unique combination of area and depth makes this survey ideal for weak lensing analyses. The CFHTLS was a joint project between Canada and France which commenced in 2003 and which is now completed. The survey area was imaged using the Megaprime wide field imager mounted at the prime focus of the Canada-France-Hawaii Telescope (CFHT) and equipped with the MegaCam camera. MegaCam comprises an array of 9×4 CCDs and has a field of view of 1 deg^2 . The wide synoptic survey covers an effective area of about 154 deg^2 in five bands: u^* , g' , r' , i' and z' . This area is composed of four independent fields, W1–4, each with an area of $23\text{--}64 \text{ deg}^2$ and with a full multi-colour depth of $i'_{AB} = 24.7$ (source in the CFHTLenS catalogue). The images have been independently reduced within the CFHTLenS collaboration, and for details on this data reduction process, we refer to Erben et al. (2009, 2012).

CFHTLenS has measured accurate shapes and photometric redshifts for 8.7×10^6 galaxies (Heymans et al. 2012; Miller et al. 2013; Hildebrandt et al. 2012). The shear estimates for the sources used in this work have been obtained using *lensfit* as detailed in Miller et al. (2013), and thoroughly tested for systematics within the CFHTLenS collaboration (see Heymans et al. 2012). All sources also have multi-band photometric redshift estimates as detailed in Hildebrandt et al. (2012). The catalogues we use in this work are discussed in Heymans et al. (2012), Miller et al. (2013) and Hildebrandt et al. (2012), with the exception of the stellar mass estimates. These estimates were obtained and tested for this paper and we therefore describe them in detail below.

2.1 Stellar masses

Our primary photometry analysis uses the Bayesian photometric redshift software BPZ (Benítez 2000; Coe et al. 2006) to estimate photometric redshifts after performing an extinction correction on the multi-colour magnitudes. Using BPZ with a simple set of six modified Coleman et al. (1980) templates is our preferred method to estimate redshifts when using only five optical bands (see Hildebrandt et al. 2012), and we note that it has been shown that the BPZ software is as accurate for photometric redshift estimates as the alternative Bayesian LEPHARE² (Arnouts et al. 1999;

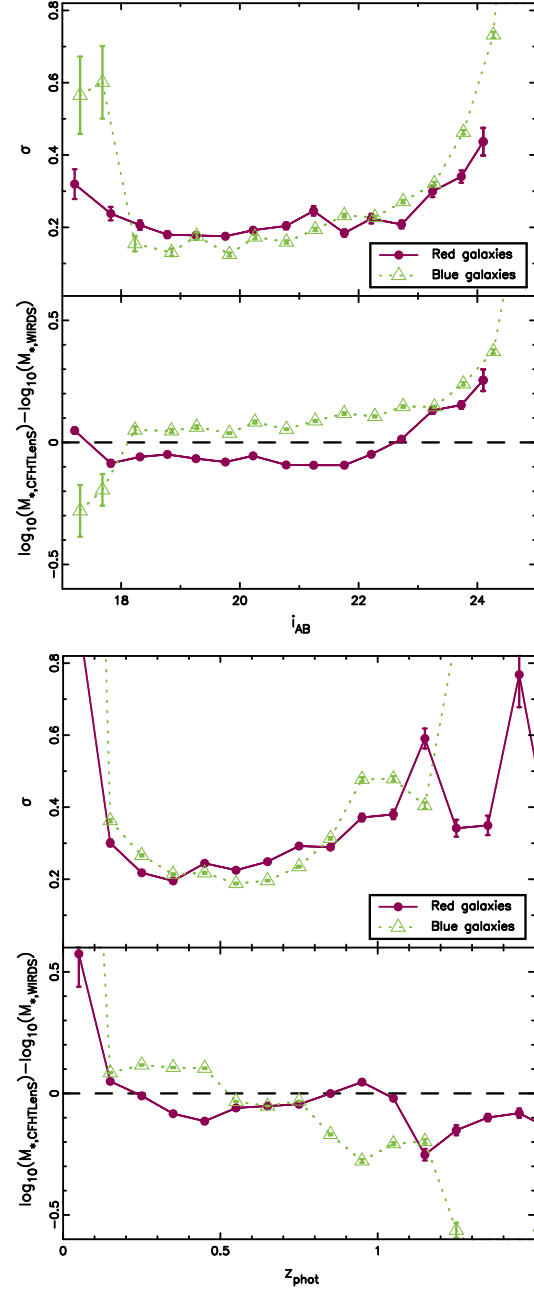


Figure 1. CFHTLenS stellar masses compared to those from the CFHT WIRCam Deep Survey (WIRDS) as a function of i'_{AB} -magnitude (top) and redshift (bottom) for red (dark purple solid dots) and blue (light green open triangles) galaxies. The upper panels in each plot show the dispersion in log stellar mass and the lower panels show the bias of the CFHTLenS stellar mass estimates relative to the WIRDS stellar mass estimates.

Ilbert et al. 2006) software (see Hildebrandt et al. 2010, for a comparison). For physical parameters such as stellar mass estimates, however, our preferred method is to use a more complex set of galaxy templates. Using LEPHARE and Bruzual & Charlot (2003) templates has been proven to be a robust method to estimate physical parameters (see Ilbert et al. 2010) and so we choose to use LEPHARE to estimate stellar masses. For a consistent analysis we also compute rest-frame luminosities from the same spectral template as used for the stellar mass estimates.

We derive our stellar mass estimates by fitting synthetic spec-

² www.cfht.hawaii.edu/~arnouts/lephare.html

tral energy distribution (SED) templates while keeping the redshift fixed at the BPZ maximum likelihood estimate. The SED templates are based on the stellar population synthesis (SPS) package developed by Bruzual & Charlot (2003) assuming a Chabrier (2003) initial mass function (IMF). Following Ilbert et al. (2010), our initial set of templates includes 18 models using two different metallicities ($Z_1 = 0.008 Z_\odot$ and $Z_2 = 0.02 Z_\odot$) and nine exponentially decreasing star formation rates $\propto e^{-t/\tau}$, where t is time and τ takes the values $\tau = 0.1, 0.3, 1, 2, 3, 5, 10, 15, 30$ Gyr. The final template set is then generated over 57 starburst ages ranging from 0.01 to 13.5 Gyr, and seven extinction values ranging from 0.05 to 0.3 using a Calzetti et al. (2000) extinction law. Ilbert et al. (2010) investigated the possible sources of uncertainty and bias by comparing stellar mass estimates between methods. The expected difference between our estimates and those based on a Salpeter IMF (Arnouts et al. 2007), a “diet” Salpeter IMF (Bell 2008), or a Kroupa IMF (Borch et al. 2006) is -0.24 dex, -0.09 dex, or 0 dex respectively (see Ilbert et al. 2010). In their Section 4.2, Ilbert et al. (2010) further argue that the choice of extinction law may lead to a systematic difference of 0.14, and the choice of SPS model to a median difference of 0.13–0.15 dex, with differences reaching 0.24 dex for massive galaxies with a high star formation rate.

We determine the errors on our stellar mass estimates via the 68% confidence limits of the SED fit, using the full probability distribution function. However, since we fix the redshift these errors tell us only how good the model fit is, and do not account for uncertainties in the photometric redshift estimates (see Section 5.2 of Hildebrandt et al. 2012). To assess the stellar mass uncertainty due to photometric redshift errors we therefore compare our mass estimates to those of the CFHT WIRCam Deep Survey (WIRDS; Bielby et al. 2012). The WIRDS stellar masses were derived from the CFHTLS Deep fields with additional broad-band near-infrared data using the same method as described here. We are thus comparing our CFHTLenS stellar mass estimates to other estimates which are also based on photometric data, but which have deeper photometry leading to a more robust stellar mass estimate. The additional near-infrared data allows us to rely on these estimates up to a redshift of 1.5 (Pozzetti et al. 2007). For our comparison we use a total of 134,290 galaxies in the overlap between the CFHTLenS and WIRDS data, splitting our sample into red and blue galaxies using their photometric type T_{BPZ} . T_{BPZ} is a number in the range of $[1.0, 6.0]$ representing the best-fit SED and we define our red and blue samples as galaxies with $T_{\text{BPZ}} < 1.5$ and $2.0 < T_{\text{BPZ}} < 4.0$ respectively, where the latter captures most spiral galaxies. A colour-colour comparison confirms that these samples are well defined. In Figure 1 we show the comparison between our stellar mass estimates and those from WIRDS as a function of magnitude (top, with galaxies in the redshift range $[0.2, 0.4]$) and redshift (bottom, with galaxies in the magnitude range $[17.0, 23.5]$).

For the range of lens redshifts used in this paper, $0.2 \leq z_{\text{lens}} \leq 0.4$, the total dispersion compared to WIRDS is then ~ 0.2 dex for both red and blue galaxies. The lower panel in the bottom plot of Figure 1 shows that for red galaxies our stellar masses are in general slightly lower than the WIRDS estimates, with the opposite being true for blue galaxies. For galaxies brighter than $i'_{\text{AB}} \sim 18$, both the dispersion and the bias increase due to biases in the redshift estimates (see Hildebrandt et al. 2012). The bias and dispersion also increase rapidly at magnitudes fainter than $i'_{\text{AB}} \sim 23$, again due to redshift errors.

We emphasise that this comparison with WIRDS quantifies only the statistical stellar mass uncertainty due to errors in the photometric redshifts and due to our particular template choice. Since

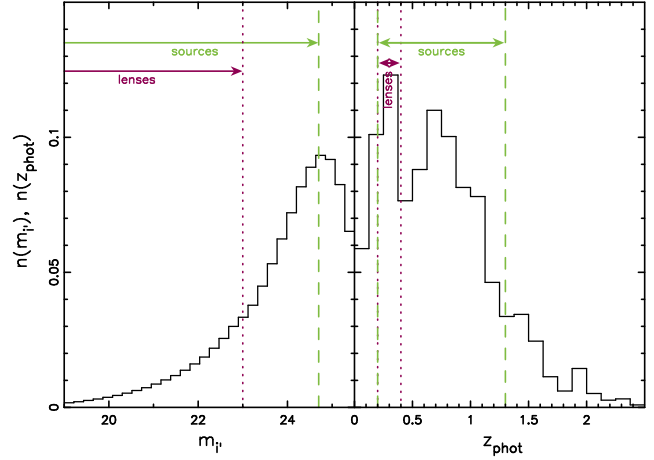


Figure 2. Magnitude (left panel) and photometric redshift (right panel) distributions of galaxies in the CFHTLenS catalogue. For the left panel we show all galaxies in the CFHTLenS, while for the right panel we limit our sample to magnitudes brighter than $i'_{\text{AB}} = 24.7$. The upper limit of lens (source) magnitude used is shown with a dark purple dotted (light green dashed) line in the left panel, while our lens (source) redshift selection is marked with dark purple dotted (light green dashed) lines in the right panel. Though the lens and source selections appear to overlap in redshift, sources are always selected such that they are well separated from lenses in redshift (see Section 2.2). Furthermore, close pairs are down-weighted as described in Section 3.1.

the mass estimates from both datasets have been derived using identical method and template set, the systematic errors affecting stellar mass estimates are not taken into account above. The uncertainties arising from the choice of models and dust extinction law adds 0.15 dex and 0.14 dex respectively to the error budget, as mentioned above, resulting in a total uncertainty of ~ 0.3 dex.

2.2 Lens and source sample

The depth of the CFHTLS enables us to investigate lenses with a large range of lens properties and redshifts, which in turn grants us the opportunity to thoroughly study the evolution of galaxy-scale dark matter haloes. As discussed by Hildebrandt et al. (2012), the use of photometric redshifts inevitably entails some bias in redshift estimates, and also in derived quantities such as luminosity and stellar mass. Our analysis is sensitive even to a small bias since our lenses are selected to reside at relatively low redshifts of $0.2 \leq z_{\text{lens}} \leq 0.4$, where z is understood to be the peak of the photometric redshift probability density function, unless explicitly stated otherwise (see Figure 2). Because our lensing signal is detected with high precision, we empirically correct for this bias using the overlap with a spectroscopic sample as described in Appendix A1. Throughout this paper, we then use the corrected redshifts, luminosities and stellar masses for our lenses. For the full survey area we achieve a lens count of $N_{\text{lens}} = 1.1 \times 10^6$.

We then split our lens sample in luminosity or stellar mass bins as described in Sections 4 and 5 to investigate the halo mass trends as a function of lens properties. Since we have access to multi-colour data, we are also able to further divide our lenses in each bin into a red and a blue sample using photometric type as described in Section 2.1. We also ensure that our lenses are brighter than $i'_{\text{AB}} < 23$ which corresponds to an 80% completeness of the spectroscopic redshift sample we use to quantify the redshift bias discussed above. The high completeness ensures that the spectro-

scopic sample is a good representation of our total galaxy sample. The galaxy sample is dominated by blue late-type galaxies for $i'_{AB} > 22$, however, and we are thus unable to perform a reliable redshift bias correction for red lenses at fainter magnitudes due to a lack of objects. We therefore exclude red lenses with $i'_{AB} > 22$ while allowing blue lenses to magnitudes as faint as $i'_{AB} = 23$. This selection is also illustrated in Figure 2.

To minimise any dilution of our lensing signal due to photometric redshift uncertainties, we follow Leauthaud et al. (2012) and use only sources for which the redshift 68% confidence limit does not overlap with the lens redshift. We further ensure that the lens and source are separated by at least 0.1 in redshift space. To verify the effectiveness of this separation, we compare the source number counts around our lenses to that around random points (as suggested by Sheldon et al. 2004, Section 4.1). This test shows no significant evidence of contamination. The source magnitude is only limited by the maximum CFHTLenS analysis depth of $i'_{AB} \sim 24.7$ (see Heymans et al. 2012; Miller et al. 2013; Hildebrandt et al. 2012). Note that we do not apply a redshift bias correction to source redshifts as there is no existing spectroscopic redshift survey at these faint limits. While it is important to correct our lenses for such a bias since the derived baryonic observables such as luminosity and stellar mass depend strongly on redshift, it is less important for the sources as the lensing signal scales with the ratio D_{ls}/D_s , where D_s and D_{ls} are the angular diameter distances to the source, and between the lens and source respectively. This ratio is insensitive to small biases in the source redshifts. Our source count for the full survey (excluding masked areas) is then $N_{\text{source}} = 5.6 \times 10^6$, corresponding to an effective source density of 10.6 arcmin^{-2} where we use the source density definition from Heymans et al. (2012, Equation 1).

The high quality of the CFHTLenS shear measurements has been verified via a series of systematics tests presented in Heymans et al. (2012) and Miller et al. (2013). To further illustrate the robustness of the shears we perform two separate analyses specifically designed to test the galaxy-galaxy lensing signal. First, we use a sample of magnitude-selected lenses across the entire survey and compare the resulting weak lensing signal to that found by Parker et al. (2007) for a 22 deg^2 subset of the CFHTLS data, and to that found by VU11 for RCS2. Both previous analyses use shear measurement software based on the class of methods first introduced by Kaiser, Squires, & Broadhurst (1995) and known as KSB. The details of the comparison may be found in Appendix B1, and we find that the signal we measure agrees well with these earlier shear measurements. The second test, as described in Appendix B2, uses the seeing of the images to test for any potential multiplicative bias still remaining. We find that this bias is consistent with zero.

3 METHOD

To analyse the dark matter haloes surrounding our lenses we use a method known as galaxy-galaxy lensing, and compare the measured signal with a halo model. In this section we will introduce the basic formalism and give an overview of our halo model.

3.1 Galaxy-galaxy lensing

The first-order lensing distortion, shear, is a stretch tangentially about a lens, induced by the foreground structure on the shape

of a background source galaxy. Assuming that sources are randomly oriented intrinsically, the net alignment caused by lensing can be measured statistically from large source samples. In a galaxy-galaxy lensing analysis, source galaxy distortions are averaged in concentric rings centred on lens galaxies. We measure the tangential shear, γ_t , as a function of radial distance from the lens this way, and also the cross shear, γ_\times , which is a 45° rotated signal. When averaged azimuthally, the cross shear can never be induced by a single lens which means that it may be used as a systematics check. The amplitude of the tangential shear is directly related to the differential surface density $\Delta\Sigma(r) = \bar{\Sigma}(< r) - \Sigma(r)$, i.e. the difference between the mean projected surface mass density enclosed by r and the surface density at r , via

$$\Delta\Sigma(r) = \Sigma_{\text{crit}} \langle \gamma_t(r) \rangle \quad (1)$$

with Σ_{crit} the critical surface density

$$\Sigma_{\text{crit}} = \frac{c^2}{4\pi G} \frac{D_s}{D_l D_{ls}} \quad (2)$$

where D_l is the angular diameter distance to the lens, and D_s and D_{ls} are defined as before. Here, c is the speed of light and G is the gravitational constant. By comparing differential surface densities rather than tangential shears, the geometric factor is neutralised and the amplitudes of the signals can be directly contrasted between different samples. The only caveat is that the properties of lenses depend on the lens redshift so this difference still has to be taken into account.

We calculate the weighted average shear in each distance bin from the lens by combining the shear measurement weight w with the geometric lensing efficiency $\eta = (D_l D_{ls})/D_s$ as described in Velander et al. (2011, Appendix B.4). By using η we down-weight close pairs and can minimise any influence of redshift inaccuracies on the measured signal that way. We quantify any remaining redshift systematics by calculating a correction factor for each mass estimate based on the redshift error distribution; see Appendix A2 for details on how this is done. The average shear, scaled to a reference redshift, is then given by

$$\langle \gamma_t(r) \rangle = \frac{\sum w_i (\gamma_{t,i} \eta_{f,i}^{-1}) \eta_{f,i}^2}{\sum w_i \eta_{f,i}^2} \quad (3)$$

where $\eta_f = \eta/\eta_{\text{ref}}$ is the lensing efficiency weight factor with η_{ref} a reference lensing efficiency value. The lensing weight w_i is defined in Equation 8 of Miller et al. (2013), and accounts both for the ellipticity measurement error and for the intrinsic shape noise. Finally, we convert the average shear to $\Delta\Sigma(r)$ using the Σ_{crit} computed for the reference lens and source redshifts.

The CFHTLenS shears are affected by a small but non-negligible multiplicative bias. Miller et al. (2013) have modelled this bias using a set of simulations specifically created as a ‘clone’ of the CFHTLenS, obtaining a calibration factor $m(\nu_{\text{SN}}, r_{\text{gal}})$ as a function of the signal-to-noise ratio, ν_{SN} , and size of the source galaxy, r_{gal} . Rather than dividing each galaxy shear by a factor $(1 + m)$, which would lead to a biased calibration as discussed in Miller et al. (2013), we apply it to our average shear measurement in each distance bin using the correction

$$1 + K(r) = \frac{\sum w_i \eta_{f,i} [1 + m(\nu_{\text{SN},i}, r_{\text{gal},i})]}{\sum w_i \eta_{f,i}} \quad (4)$$

The lensing signal is then calibrated as follows:

$$\langle \gamma^{\text{cal}}(r) \rangle = \frac{\langle \gamma(r) \rangle}{1 + K(r)} \quad (5)$$

The effect of this correction term on our galaxy-galaxy analysis is to increase the average lensing signal amplitude by at most 6%. Though there will be some uncertainty associated with this term, Kilbinger et al. (2013) find that it has a negligible effect on their shear covariance matrix. The calibration factor m enters linearly in our Equation 5, while it is squared in the Kilbinger et al. (2013) correlation function correction factor, thus amplifying its effect. The conclusion we draw is therefore that the impact of the calibration factor uncertainty will be insignificant in this work. We also apply the additive c -term correction discussed in Heymans et al. (2012) but find that it does not change our results either.

The circular averaging over lens-source pairs makes this type of analysis robust against small-scale systematics introduced by for example PSF residuals in the shape measurement catalogues. Because the galaxy-galaxy lensing signal is more resilient to systematics than cosmic shear, we choose to maximise our signal-to-noise by using the full CFHTLenS area (except for masked areas) rather than removing the fields that have not passed the cosmic shear systematics test described in Heymans et al. (2012). However, there could be spurious large-scale signal present owing to areas being masked, or from lenses close to an edge, such that the circular average does not cover all azimuthal angles. We correct for such spurious signal using a catalogue of random lens positions situated outside any masked areas; the number of random lenses used is 50,000 per square-degree field, which amounts to more than ten times as many as real lenses. The stacked lensing signal measured around these random lenses is evidence of incomplete circular averages and will be present in the observed stacked lensing signal as well. Because of our high sampling of this random points signal, we can correct the observed signal measured in each field by subtracting the signal around the random lenses. This random points test is discussed in more detail in Mandelbaum et al. (2005a). The test shows that for this data, individual fields do indeed display a signal around random lenses which is to be expected, even in the absence of any shapemeasurement error, due to cosmic shear and shot noise, and due to the masking effect mentioned above. Averaged over the entire CFHTLenS area the random lens signal is insignificant relative to the signal around true lenses ranging from $\sim 0.5\%$ to $\sim 5\%$ over the angular range used in this analysis. Additionally, to ascertain whether including the fields that fail the cosmic shear systematics test biases our results, we compare the tangential shear around all galaxies with $19.0 < i'_{AB} < 22.0$ in the fields that respectively pass and fail this test, and find no significant differences between the signals.

3.2 The halo model

To accurately model the weak lensing signal observed around galaxy-size haloes, we have to account for the fact that galaxies generally reside in clustered environments. In this work we do this by employing the halo model software first introduced in VU11. For full details on the exact implementation we refer to VU11; here we give a qualitative overview.

Our halo model builds on work presented in Guzik & Seljak (2002) and Mandelbaum et al. (2005b), where the full lensing signal is modelled by accounting for the central galaxies and their satellites separately. We assume that a fraction $(1-\alpha)$ of our galaxy sample reside at the centre of a dark matter halo, and the remaining objects are satellite galaxies surrounded by subhaloes which in turn reside inside a larger halo. In this context α is the satellite fraction of a given sample.

The lensing signal induced by central galaxies consists of two

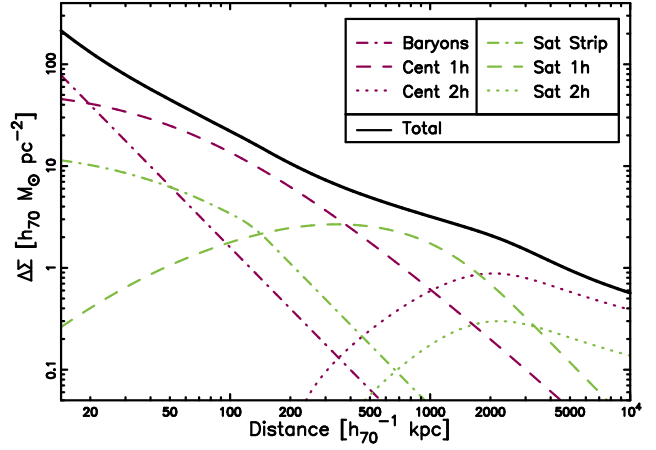


Figure 3. Illustration of the halo model used in this paper. Here we have used a halo mass of $M_{200} = 10^{12} h_{70}^{-1} M_{\odot}$, a stellar mass of $M_{*} = 5 \times 10^{10} h_{70}^{-2} M_{\odot}$ and a satellite fraction of $\alpha = 0.2$. The lens redshift is $z_{\text{lens}} = 0.5$. Dark purple lines represent quantities tied to galaxies which are centrally located in their haloes while light green lines correspond to satellite quantities. The dark purple dash-dotted line is the baryonic component, the light green dash-dotted line is the stripped satellite halo, dashed lines are the 1-halo components induced by the main dark matter halo and dotted lines are the 2-halo components originating from nearby haloes.

components: the signal arising from the main dark matter halo (the 1-halo term $\Delta\Sigma^{1h}$) and the contribution from neighbouring haloes (the 2-halo term $\Delta\Sigma^{2h}$). The two components simply add to give the lensing signal due to central galaxies:

$$\Delta\Sigma_{\text{cent}} = \Delta\Sigma_{\text{cent}}^{1h} + \Delta\Sigma_{\text{cent}}^{2h} . \quad (6)$$

In our model we assume that all main dark matter haloes are well represented by an NFW density profile (Navarro, Frenk, & White 1996) with a mass-concentration relationship as given by Duffy et al. (2008). The halo model parameters resulting from an analysis such as ours (see, for example, Section 4) are not very sensitive to the exact halo concentration, however, as discussed in VU11. To compute the 2-halo term, we use the non-linear power spectrum from Smith et al. (2003). We also assume that the dependence of the galaxy bias on mass follows the prescription from Sheth et al. (2001), incorporating the adjustments described in Tinker et al. (2005). Note that this mass-bias relation is empirically calibrated on large numerical simulations, and does not discriminate between different galaxy types. The bias prescription we adopt for our halo model does not include non-linear effects. Figure 1 from Mandelbaum et al. (2012) shows that non-linear bias affects the galaxy-dark matter cross-correlation coefficient at the 2% level at a comoving separation of $4 h_{70}^{-1}$ Mpc. The magnitude of the effect diminishes with increasing distance to 1% at $10 h_{70}^{-1}$ Mpc, and the influence on our 2-halo terms should be comparable. The affected regime, where the 1-halo and 2-halo terms overlap, is notoriously difficult to model however. One major issue is that of halo exclusion which attempts to account for the way neighbouring dark matter haloes overlap. Since the effect of non-linearity is likely small compared to other modelling uncertainties on these scales, and since the affected range is beyond that used to determine halo masses in this paper (see Section 4), we choose not to include non-linear biasing in our model. Finally, we note that the central term essentially assumes a delta function in halo mass as a function of a given observable since we do not integrate over the halo mass distribution. For a given luminosity bin, for example, the particu-

lar mass distribution within that bin therefore has to be accounted for. We do correct our measured halo mass for this in the following sections, assuming a log-normal distribution, and the correction method is described in Appendices A2 and A3 for the luminosity and stellar mass analysis respectively.

We model satellite galaxies as residing in subhaloes whose spatial distribution follows the dark matter distribution of the main halo. The number density of satellites in a halo of a given mass is described by the halo occupation distribution (HOD) which is commonly parameterised through a power law of the form $\langle N \rangle = M^\epsilon$. Following Mandelbaum et al. (2005b), we set $\epsilon = 1$ for masses above a characteristic mass scale, defined to be three times the typical halo mass of a set of lenses. For masses below this threshold, we use $\epsilon = 2$. In our model, the subhaloes have been tidally stripped of dark matter in the outer regions. As Mandelbaum et al. (2005b) did, we adopt a truncated NFW profile, choosing a truncation radius of $0.4r_{200}$ beyond which the lensing signal is proportional to r^{-2} , where r is the physical distance from the lens. This choice results in about 50% of the subhalo dark matter being stripped, and we acquire a satellite term which supplies signal on small scales. Thus satellite galaxies add three further components to the total lensing signal: the contribution from the stripped subhalo ($\Delta\Sigma^{\text{strip}}$), the satellite 1-halo term which is off-centre since the satellite galaxy is not at the centre of the main halo, and the 2-halo term from nearby haloes. Just as for the central galaxies, the three terms add to give the satellite lensing signal:

$$\Delta\Sigma_{\text{sat}} = \Delta\Sigma_{\text{sat}}^{\text{strip}} + \Delta\Sigma_{\text{sat}}^{\text{1h}} + \Delta\Sigma_{\text{sat}}^{\text{2h}}. \quad (7)$$

There is an additional contribution to the lensing signal, not yet considered in the above equations. This is the signal induced by the lens baryons ($\Delta\Sigma^{\text{bar}}$). This last term is a refinement of the halo model presented in VU11, necessary since weak lensing measures the total mass of a system and not just the dark matter mass. Following Leauthaud et al. (2011) we model the baryonic component as a point source with a mass equal to the mean stellar mass of the lenses in the sample:

$$\Delta\Sigma^{\text{bar}} = \frac{\langle M_* \rangle}{\pi r^2}. \quad (8)$$

This term is fixed by the stellar mass of the lens, and we do not fit it. Note that we choose not to include the baryonic term for neighbouring haloes, but its contribution is negligible.

Finally, to obtain the total lensing signal of a galaxy sample of which a fraction α are satellites we combine the baryon, central and satellite galaxy signals, applying the appropriate proportions:

$$\Delta\Sigma = \Delta\Sigma^{\text{bar}} + (1 - \alpha)\Delta\Sigma_{\text{cent}} + \alpha\Delta\Sigma_{\text{sat}}. \quad (9)$$

All components of our halo model are illustrated in Figure 3. In this example the dark matter halo mass is $M_{200} = 10^{12} h_{70}^{-1} M_\odot$, the stellar mass is $M_* = 5 \times 10^{10} h_{70}^{-2} M_\odot$, the satellite fraction is $\alpha = 0.2$, the lens redshift is $z_{\text{lens}} = 0.5$ and $D_{ls}/D_s = 0.5$. On small scales the 1-halo components are prominent, while on large scales the 2-halo components dominate.

The halo model is necessarily based on a number of assumptions (such as the spatial distribution of satellites, the HOD choice, the mass-concentration relation, the bias prescription and the adopted cosmology parameters), some of which may be overly stringent or inaccurate. Ideally, uncertainties should be assigned to these assumptions and included in the final fit parameter error budget. Alas, reliable error estimates for these assumptions are not yet available in literature. To fully investigate the model assumptions would require the use of high-resolution hydrodynamical simula-

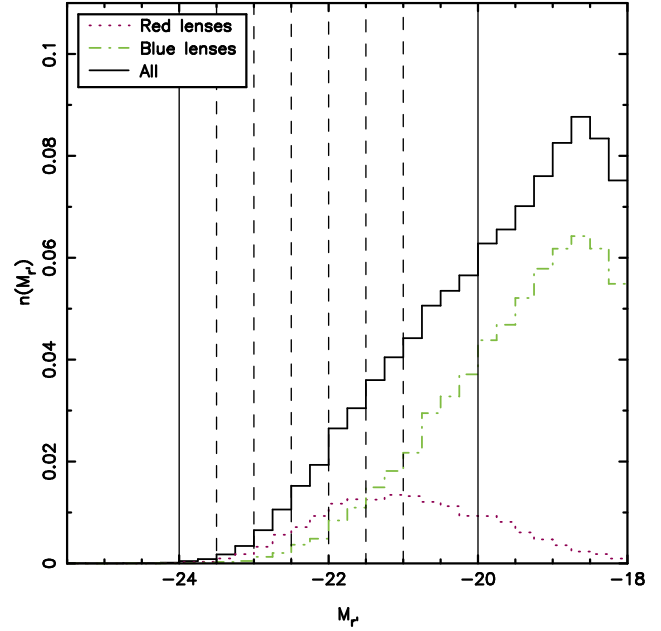


Figure 4. r' -band absolute magnitude distribution in the CFHTLenS catalogues for lenses with redshifts $0.2 \leq z_{\text{lens}} \leq 0.4$ (black solid histogram). The distribution of red (blue) lenses is shown in dotted dark purple (dot-dashed light green). Our lens bins are marked with vertical lines.

Table 1. Details of the luminosity bins. (1) Absolute magnitude range; (2) Number of lenses; (3) Mean redshift; (4) Fraction of lenses that are blue.

Sample	$M_{r'}^{(1)}$	$n_{\text{lens}}^{(2)}$	$\langle z \rangle^{(3)}$	$f_{\text{blue}}^{(4)}$
L1	[-21.0,-20.0]	91224	0.32	0.70
L2	[-21.5,-21.0]	33633	0.32	0.45
L3	[-22.0,-21.5]	23075	0.32	0.32
L4	[-22.5,-22.0]	12603	0.32	0.20
L5	[-23.0,-22.5]	5344	0.32	0.11
L6	[-23.5,-23.0]	1704	0.31	0.05
L7	[-24.0,-23.5]	344	0.30	0.03
L8	[-24.5,-24.0]	76	0.30	0.09

tions, and that is beyond the scope of this work. We therefore note that the results we obtain are specific to the adopted halo model, and any differences with alternative models should be accounted for when comparing our results to other work. This is likely to have more of an effect on the satellite fraction than on the measured halo masses though, since the above assumptions mainly affect the model on scales beyond the range of the central 1-halo term. Additionally, the errors on the derived halo masses and satellite fractions in this work may be slightly underestimated due to the exclusion of modelling uncertainties.

4 LUMINOSITY TREND

The luminosity of a galaxy is an easily obtainable indicator of its baryonic content. To investigate the relation between dark matter halo mass and galaxy mass we therefore split the lenses into 8 bins according to MegaCam absolute r' -band magnitudes as detailed in Table 1 and illustrated in Figure 4. The lens property averages quoted in this and forthcoming tables are pure averages and do not

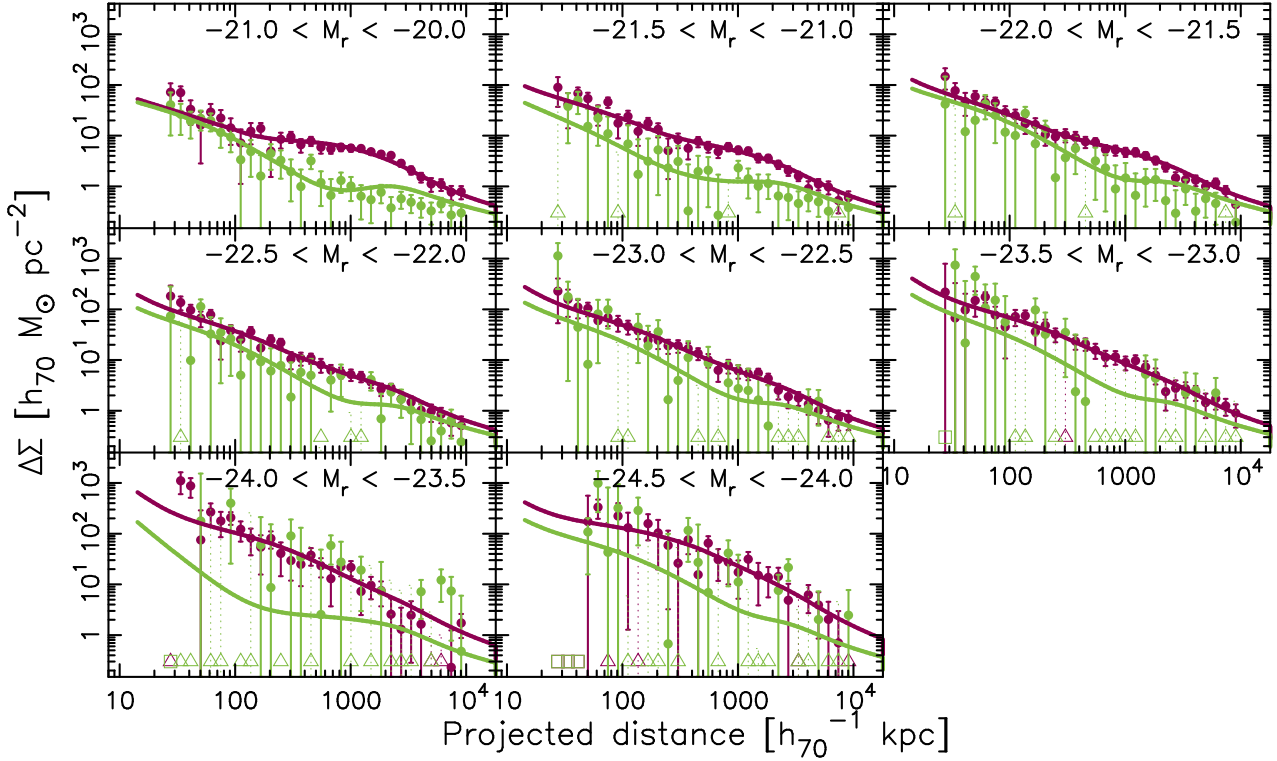


Figure 5. Galaxy-galaxy lensing signal around lenses which have been split into luminosity bins according to Table 1, modelled using the halo model described in Section 3.2. The dark purple (light green) dots represent the measured differential surface density, $\Delta\Sigma$, of the red (blue) lenses, and the solid line is the best-fit halo model. Triangles represent negative points that are included unaltered in the model fitting procedure, but that have here been moved up to positive values as a reference. The dotted error bars are the unaltered error bars belonging to the negative points. The squares represent distance bins containing no objects. For a detailed decomposition into the halo model components, we refer to Appendix C.

include the lensing weights, unless explicitly specified. The choice of bin limits follows the lens selection in VU11. This choice will allow us to directly compare our results to the results shown in VU11 since the RCS2 data have been obtained using the same filters and telescope. We also split each luminosity bin into red and blue subsamples as described in Section 2.1 and proceed to measure the galaxy-galaxy lensing signal for each sample, with errors obtained via bootstrapping 10^4 times over the full CFHTLenS area, where the number of bootstraps ensure convergence of the mean. We then fit the signal between $50 h_{70}^{-1}$ kpc and $2 h_{70}^{-1}$ Mpc with our halo model using a χ^2 analysis. Only the halo mass M_{200} and the satellite fraction α are left as free parameters while we keep all other variables fixed. When fitting, we assume that the covariance matrix of the lensing measurements is diagonal. Off-diagonal elements are generally present due to cosmic variance and shape noise, but Choi et al. (2012) find that for a lens sample at a redshift range similar to that of our lenses the covariance matrix is diagonal up to ~ 1 Mpc, which corresponds well to the largest scale we include in our fits (this is also confirmed via visual inspection of our matrices). Furthermore, Figure 7.2 from the PhD thesis of Jens Rödiger³ shows that the off-diagonal elements are comparatively small. Hence we do not expect that the off-diagonal elements in the χ^2 fit will have a significant impact on the best-fit parameters. The results are shown in Figure 5 for all luminosity bins and for each red and blue lens sample, with details of the fitted halo model parameters quoted in Table 2. The halo masses in this table have

been corrected for various contamination effects as detailed in Section 4.1 and Appendix A. Note that the number of blue lenses in the two highest-luminosity bins, L7 and L8, is too low to adequately constrain the halo mass. In the following sections, these two blue bins have therefore been removed from the analysis of blue lenses.

As expected, the amplitude of the signal increases with luminosity for both red and blue samples indicating an increased halo mass. In general, for identical luminosity selections blue galaxies have less massive haloes than red galaxies do. For the red sample, lower luminosity bins display a slight bump at scales of $\sim 1 h_{70}^{-1}$ Mpc. This is due to the satellite 1-halo term becoming important and indicates that a significant fraction of the galaxies in those bins are in fact satellite galaxies inside a larger halo. On the other hand, brighter red galaxies are more likely to be located centrally in a halo. The blue galaxy halo models also display a bump for the lower luminosity bins, but this feature is at larger scales than the satellite 1-halo term. The signal breakdown shown in Figure C2 (Appendix C) reveals that this bump is due to the central 2-halo term arising from the contribution of nearby haloes. We note, however, that in these low-luminosity blue bins, the model overestimates the signal at projected separations greater than $\sim 2 h_{70}^{-1}$ Mpc. This could be an indicator that our description of the galaxy bias, while accurate for red lenses, results in too high a bias for blue lenses. Alternatively, the discrepancy may suggest that the regime where the 1-halo term transitions into the 2-halo term is not accurately described due to inherent limitations of the halo model, such as non-linear galaxy biasing, halo exclusion representation and inaccuracies in the non-linear matter power spectrum (see Section 3.2). To optimally model the regime in question, the handling

³ <http://hss.ulb.uni-bonn.de/2009/1790/1790.htm>

Table 2. Results from the halo model fit for the luminosity bins. (1) Mean luminosity for red lenses [$10^{10} h_{70}^{-2} L_{\odot}$]; (2) Mean stellar mass for red lenses [$10^{10} h_{70}^{-2} M_{\odot}$]; (3) Scatter-corrected best-fit halo mass for red lenses [$10^{11} h_{70}^{-1} M_{\odot}$]; (4) Best-fit satellite fraction for red lenses; (5) Mean luminosity for blue lenses [$10^{10} h_{70}^{-2} L_{\odot}$]; (6) Mean stellar mass for blue lenses [$10^{10} h_{70}^{-2} M_{\odot}$]; (7) Scatter-corrected best-fit halo mass for blue lenses [$10^{11} h_{70}^{-1} M_{\odot}$]; (8) Best-fit satellite fraction for blue lenses. The fitted parameters are quoted with their 1σ errors. Note that the blue results from the L7 and L8 bins are not used for fitting the power law relation in Section 4.1.

Sample	$\langle L_r^{\text{red}} \rangle^{(1)}$	$\langle M_*^{\text{red}} \rangle^{(2)}$	$M_h^{\text{red}}^{(3)}$	$\alpha^{\text{red}}^{(4)}$	$\langle L_r^{\text{blue}} \rangle^{(5)}$	$\langle M_*^{\text{blue}} \rangle^{(6)}$	$M_h^{\text{blue}}^{(7)}$	$\alpha^{\text{blue}}^{(8)}$
L1	0.91	1.83	$3.08^{+0.98}_{-0.95}$	$0.54^{+0.05}_{-0.04}$	1.08	0.50	$3.72^{+0.65}_{-0.70}$	$0.00^{+0.02}_{-0.00}$
L2	1.74	3.74	$10.3^{+2.37}_{-1.73}$	$0.35^{+0.04}_{-0.04}$	2.23	1.10	$1.83^{+1.35}_{-1.05}$	$0.07^{+0.04}_{-0.04}$
L3	2.73	5.97	$15.5^{+2.72}_{-2.31}$	$0.31^{+0.04}_{-0.04}$	3.52	1.83	$11.2^{+3.22}_{-2.50}$	$0.00^{+0.03}_{-0.00}$
L4	4.28	9.35	$34.3^{+6.00}_{-4.43}$	$0.21^{+0.04}_{-0.05}$	5.51	3.00	$13.0^{+4.13}_{-4.40}$	$0.00^{+0.06}_{-0.00}$
L5	6.69	14.9	$60.7^{+5.90}_{-6.64}$	$0.20^{+0.00}_{-0.03}$	8.44	4.63	$16.3^{+11.4}_{-9.34}$	$0.00^{+0.12}_{-0.00}$
L6	10.4	23.9	$123^{+15.2}_{-16.0}$	$0.20^{+0.00}_{-0.04}$	13.7	7.88	$23.3^{+26.5}_{-18.9}$	$0.00^{+0.14}_{-0.00}$
L7	16.4	35.6	$344^{+70.4}_{-89.6}$	$0.06^{+0.14}_{-0.06}$	—	—	—	—
L8	25.4	20.3	762^{+320}_{-154}	$0.20^{+0.00}_{-0.20}$	—	—	—	—

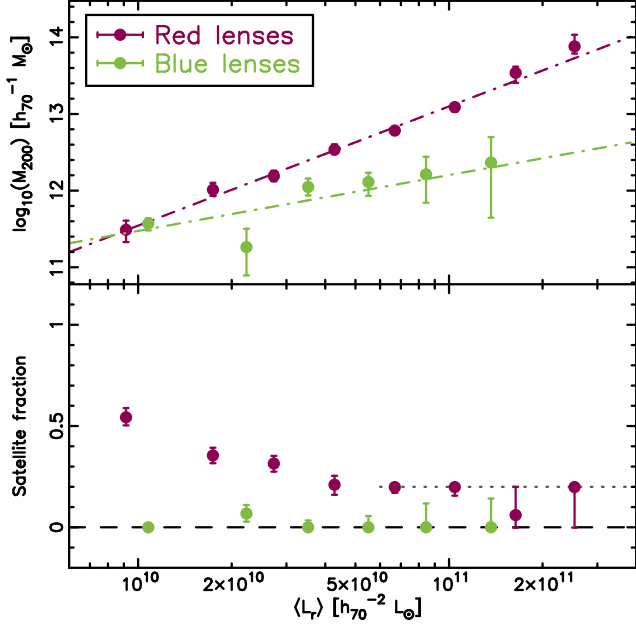


Figure 6. Satellite fraction α and bias-corrected halo mass M_{200} as a function of r' -band luminosity. Dark purple (light green) dots represent the results for red (blue) lens galaxies, and the dash-dotted lines show the power law scaling relations fit to the Figure 5 galaxy-galaxy lensing signal (rather than to the points shown) as described in the text. The dotted line in the lower panel shows the α prior applied to the highest-luminosity bins.

of these factors should perhaps be dependent on galaxy type, but that is not done here. The reason is that we do not currently have enough data available to investigate this regime in detail. In the future, however, it should be explored further.

4.1 Luminosity scaling relations

Before determining the relation between halo mass and luminosity we have to correct our raw halo mass estimates for two systematic effects. Firstly, we rely on photometric redshift estimates which do not benefit from the absolute accuracy of spectroscopic redshifts. We can therefore not be certain that a lens which is thought to be at a certain redshift is in fact at that redshift. If the redshift is different, then the derived luminosity will also be different which means that

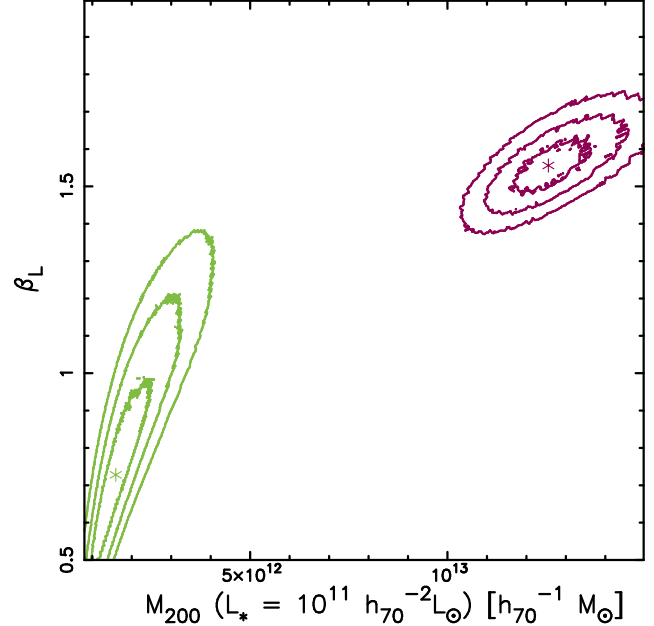


Figure 7. Constraints on the power law fits shown in Figure 6. In dark purple (light green) we show the constraints on the fit for red (blue) lenses, with lines representing the 67.8%, 95.4% and 99.7% confidence limits and stars representing the best-fit value.

the lens may have been placed in the wrong bin. Though the lenses can scatter randomly according to their individual redshift errors, the net effect will be to scatter lenses from bins with higher abundances to those with lower abundances. The measured halo mass will therefore be biased. To correct for this effect we create mock lens catalogues and allow the objects to scatter according to their redshift error distributions. Secondly, the halo masses in a given luminosity bin will not be evenly distributed, which means that the measured halo mass does not necessarily correspond to the mean halo mass. The derivation of the factor we apply to our halo masses to correct for both these effects is detailed in Appendix A2.

The estimated halo masses for all luminosity bins, corrected for the above scatter effects, are shown as a function of luminosity in the top panel of Figure 6. Red lenses display a steeper relationship between halo mass and luminosity than blue lenses, and the

haloes of the blue galaxies are in general less massive for a given luminosity bin. Following VU11, we fit a power law of the form

$$M_{200} = M_{0,L} \left(\frac{L}{L_{\text{fid}}} \right)^{\beta_L} \quad (10)$$

with $L_{\text{fid}} = 10^{11} h_{70}^{-2} L_{r',\odot}$ a scaling factor chosen to be the r' -band luminosity of a fiducial galaxy. Rather than fitting to the final mass estimates we fit this relation directly to the lensing signals themselves (taking the scatter correction into account). We do this because the error bars are asymmetric in the former case, but the difference in results between the two fitting techniques is small.

For our red lenses we find $M_{0,L} = 1.26^{+0.07}_{-0.06} \times 10^{13} h_{70}^{-1} M_{\odot}$ and $\beta_L = 1.56^{+0.04}_{-0.06}$, while for our blue lenses the corresponding numbers are $M_{0,L} = 0.16 \pm 0.03 \times 10^{13} h_{70}^{-1} M_{\odot}$ and $\beta_L = 0.73^{+0.09}_{-0.08}$. The parameters are quoted with their 1σ errors and the constraints for these fits are shown in Figure 7. Here we again see that the red lenses are better constrained than the blue. This is partly because we have more red lenses in most bins, and partly because red lenses in general are more massive at a given luminosity.

The mass-to-light ratios, $M_{200}/\langle L_r \rangle$, of our red sample range from $34^{+11}_{-10} h_{70} M_{\odot} L_{\odot}^{-1}$, at the lowest luminosity bin to $91^{+9}_{-10} h_{70} M_{\odot} L_{\odot}^{-1}$ for L5. For our blue sample the numbers are $34 \pm 11 h_{70} M_{\odot} L_{\odot}^{-1}$ for L1 and $19 \pm 2 h_{70} M_{\odot} L_{\odot}^{-1}$ for L5. Beyond L5, the mass-to-light ratio continues to increase, reaching $300^{+126}_{-61} h_{70} M_{\odot} L_{\odot}^{-1}$ for red lenses in bin L8. In these highest luminosity bins a significant fraction of the red lenses may be associated with groups or small clusters, as pointed out by VU11.

4.2 Satellite fraction

The lower panel of Figure 6 shows the satellite fraction α as a function of luminosity for both the red and the blue sample. At lower luminosities the satellite fraction is $\sim 50\%$ for red lenses and as the luminosity increases the satellite fraction decreases. This indicates that a large number of faint red lenses are satellites inside a larger dark matter halo, consistent with previous findings (see Mandelbaum et al. 2006; van Uitert et al. 2011; Coupon et al. 2012). In the highest luminosity bins the satellite fraction is difficult to constrain due to the shape of the halo model satellite terms (light green lines in Figure 3) becoming indistinguishable from the central 1-halo term (dark purple dashed), as discussed in Appendix C. To ensure that our halo masses are not biased low we follow VU11 and apply a uniform satellite fraction prior to these bins, allowing a maximum α of 20%. This prior is marked in Figure 6. For blue lenses, the satellite fraction remains low across all luminosities indicating that almost none of our blue galaxies are satellites, again consistent with previous findings. This may be a sign that blue galaxies in our analysis are in general more isolated than red ones for a given luminosity, a theory corroborated by the low signal on large scales for blue galaxies (see Figure C2 in Appendix C). Here we have made no distinction between field galaxies and galaxies residing in a denser environment; for a more in-depth study of this distinction see Gillis et al. (2013).

5 STELLAR MASS TREND

The galaxy luminosity as a tracer of baryonic content depends both on age and on star formation history. A galaxy's stellar mass does not have such dependence and may therefore be a better indicator

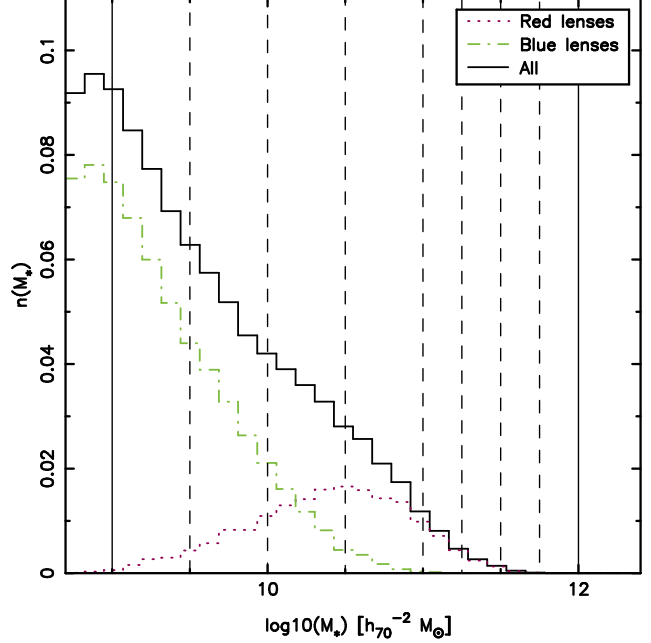


Figure 8. Stellar mass distribution in the CFHTLenS catalogues for lenses with redshifts $0.2 \leq z_{\text{lens}} \leq 0.4$ (black solid histogram). The distribution of red (blue) lenses is shown in dotted dark purple (dot-dashed light green). Our lens bins are marked with vertical lines.

Table 3. Details of the stellar mass bins. (1) Stellar mass range $[h_{70}^{-2} M_{\odot}]$; (2) Number of lenses; (3) Mean redshift; (4) Fraction of lenses that are blue.

Sample	$\log_{10} M_*$ ⁽¹⁾	n_{lens} ⁽²⁾	$\langle z \rangle$ ⁽³⁾	f_{blue} ⁽⁴⁾
S1	[9.00,9.50]	126406	0.33	0.981
S2	[9.50,10.00]	78283	0.32	0.828
S3	[10.00,10.50]	48957	0.32	0.391
S4	[10.50,11.00]	37365	0.32	0.043
S5	[11.00,11.25]	7474	0.32	0.003
S6	[11.25,11.50]	2447	0.31	0.001
S7	[11.50,11.75]	396	0.30	0.000
S8	[11.75,12.00]	12	0.31	0.000

of its baryonic content. In this section we study the relation between galaxy stellar mass and the dark matter halo mass, dividing the lenses into 9 stellar mass bins as illustrated in Figure 8 with details in Table 3. As we did for the luminosity analysis (Section 4) we further split each stellar mass bin into a red and a blue sample using their photometric types to approximate early- and late-type galaxies.

We measure the galaxy-galaxy lensing signal for each sample as before, and fit on scales between $50 h_{70}^{-1} \text{ kpc}$ and $2 h_{70}^{-1} \text{ Mpc}$ using our halo model with the halo mass M_{200} and the satellite fraction α as free parameters. Similarly to the previous section, the results are shown in Figure 9 for all stellar mass bins and for each red and blue lens sample, with details of the fitted halo model parameters quoted in Table 4. There are no blue lenses available in the two highest stellar mass bins, and in bins S5 and S6 the number of blue lenses is too low to constrain the signal. We therefore remove them from our analysis in the following sections.

The mean mass in each bin increases with increasing stellar mass as expected, resulting in an increased signal amplitude. Simi-

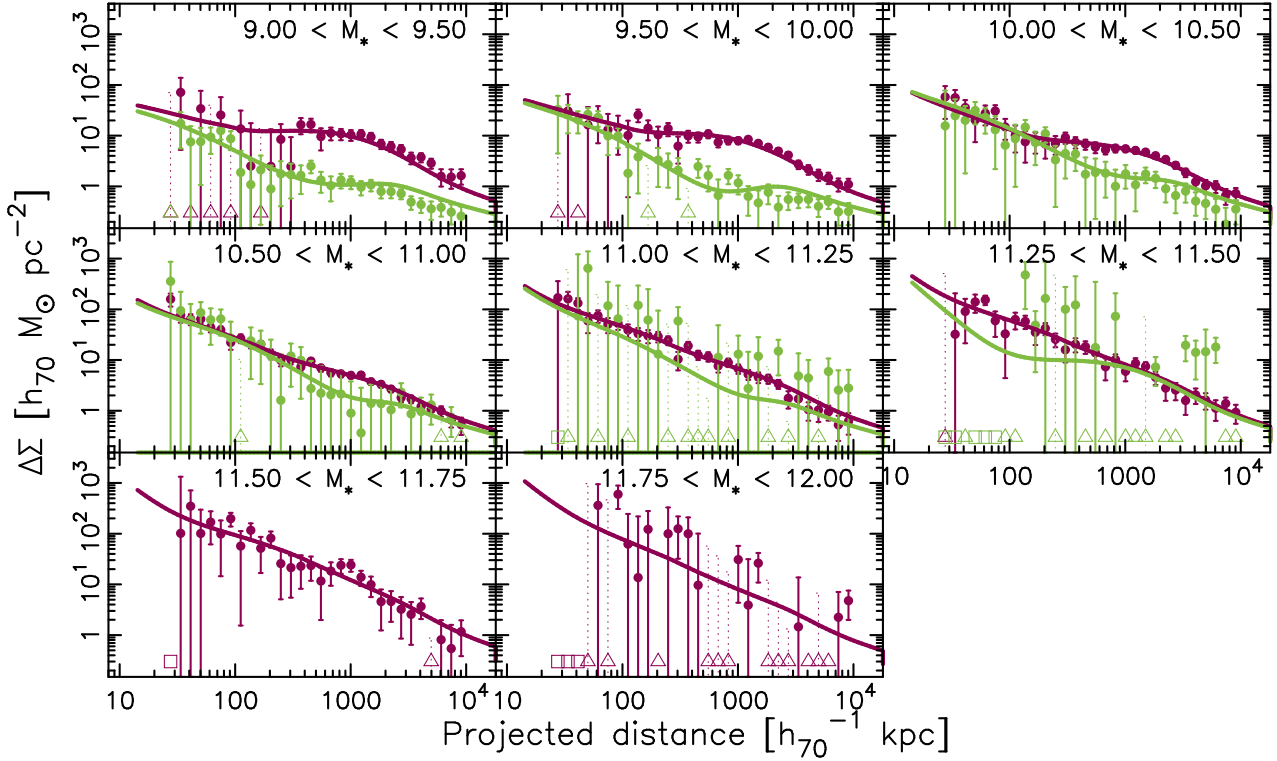


Figure 9. Galaxy-galaxy lensing signal around lenses which have been split into stellar mass bins according to Table 3, modelled using the halo model described in Section 3.2. The dark purple (light green) dots represent the measured differential surface density, $\Delta\Sigma$, of the red (blue) lenses, and the solid line is the best-fit halo model. Triangles represent negative points that are included unaltered in the model fitting procedure, but that have here been moved up to positive values as a reference. The dotted error bars are the unaltered error bars belonging to the negative points. The squares represent distance bins containing no objects. For a detailed decomposition into the halo model components, we refer to Appendix D.

Table 4. Results from the halo model fit for the stellar mass bins. (1) Mean luminosity for red lenses [$10^{10} h_{70}^{-2} L_{\odot}$]; (2) Mean stellar mass for red lenses [$10^{10} h_{70}^{-2} M_{\odot}$]; (3) Scatter-corrected best-fit mean halo mass for red lenses [$10^{11} h_{70}^{-1} M_{\odot}$]; (4) Best-fit satellite fraction for red lenses; (5) Mean luminosity for blue lenses [$10^{10} h_{70}^{-2} L_{\odot}$]; (6) Mean stellar mass for blue lenses [$10^{10} h_{70}^{-2} M_{\odot}$]; (7) Scatter-corrected best-fit mean halo mass for blue lenses [$10^{11} h_{70}^{-1} M_{\odot}$]; (8) Best-fit satellite fraction for blue lenses. The fitted parameters are quoted with their 1σ errors. Note that the red results from the S1 and S2 bins, and the blue results from the S5 and S6 bins, are not used for fitting the power law relation in Section 5.1.

Sample	$\langle L_r^{\text{red}} \rangle^{(1)}$	$\langle M_*^{\text{red}} \rangle^{(2)}$	$M_h^{\text{red}}^{(3)}$	$\alpha^{\text{red}}^{(4)}$	$\langle L_r^{\text{blue}} \rangle^{(5)}$	$\langle M_*^{\text{blue}} \rangle^{(6)}$	$M_h^{\text{blue}}^{(7)}$	$\alpha^{\text{blue}}^{(8)}$
S1	0.22	0.23	$1.68^{+0.99}_{-0.65}$	$1.00^{+0.00}_{-0.03}$	0.41	0.18	$1.96^{+0.51}_{-0.44}$	$0.05^{+0.02}_{-0.02}$
S2	0.44	0.66	$2.93^{+1.50}_{-1.16}$	$0.82^{+0.07}_{-0.07}$	1.11	0.54	$3.91^{+0.79}_{-0.73}$	$0.00^{+0.02}_{-0.00}$
S3	1.06	1.97	$3.58^{+1.03}_{-0.99}$	$0.51^{+0.04}_{-0.04}$	2.87	1.59	$10.2^{+2.63}_{-2.28}$	$0.05^{+0.03}_{-0.03}$
S4	2.46	5.65	$20.9^{+2.57}_{-1.86}$	$0.31^{+0.03}_{-0.03}$	7.07	4.29	$30.9^{+12.8}_{-9.53}$	$0.00^{+0.05}_{-0.00}$
S5	5.38	13.0	$70.5^{+10.5}_{-10.5}$	$0.30^{+0.05}_{-0.06}$	—	—	—	—
S6	8.96	22.6	$145^{+29.5}_{-30.0}$	$0.28^{+0.09}_{-0.09}$	—	—	—	—
S7	14.3	38.6	$459^{+94.8}_{-71.0}$	$0.20^{+0.00}_{-0.07}$	—	—	—	—
S8	19.1	62.7	264^{+432}_{-243}	$0.20^{+0.00}_{-0.20}$	—	—	—	—

lar to the luminosity samples in the previous section, the red lower-mass bins display a bump at scales of $\sim 0.5 h^{-1} \text{Mpc}$. Here the lowest bins contain less massive galaxies than the lowest luminosity bins and the bump is more pronounced, indicating that most of the galaxies in these low-mass samples are satellite galaxies. The contribution from nearby haloes is again clearly visible in the best-fit halo model of the lower-mass blue samples, though as noted in Section 4, this may be due to an inaccurate galaxy bias description for blue lenses.

5.1 Stellar mass scaling relations

Just as for the luminosity bins, we have to correct the halo mass estimates for two scatter effects: one due to errors in the stellar mass estimates and another due to halo masses not being evenly distributed within a given bin. We describe the correction for these effects in Appendix A3. The best-fit halo masses, once corrected for these scatter effects, and satellite fractions α for each stellar mass bin are shown in Figure 10. In the lower-mass bins, nearly all red lenses are satellites while for higher masses, the majority are located centrally in their halo. As discussed in Section 4.2, this

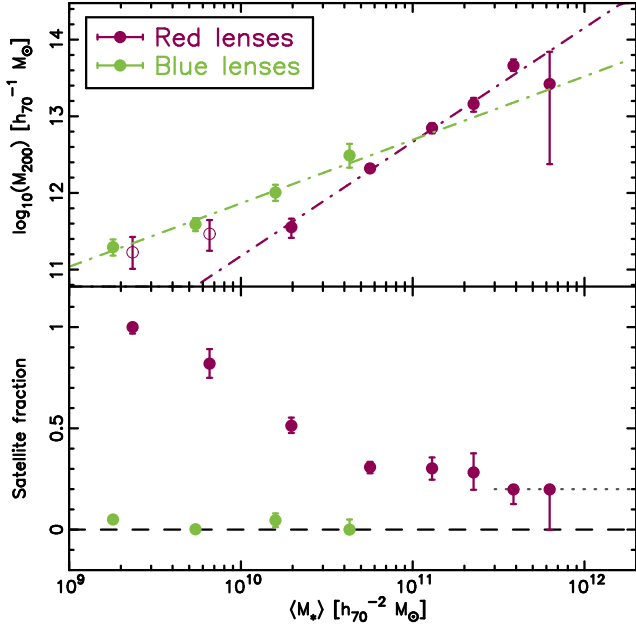


Figure 10. Satellite fraction α and halo mass M_{200} as a function of stellar mass. Dark purple (light green) dots represent the results for red (blue) lens galaxies. Open circles show the points that have been excluded from the power law fit because of a high satellite fraction. The dotted line in the lower panel shows the α prior applied to the highest-stellar mass bins.

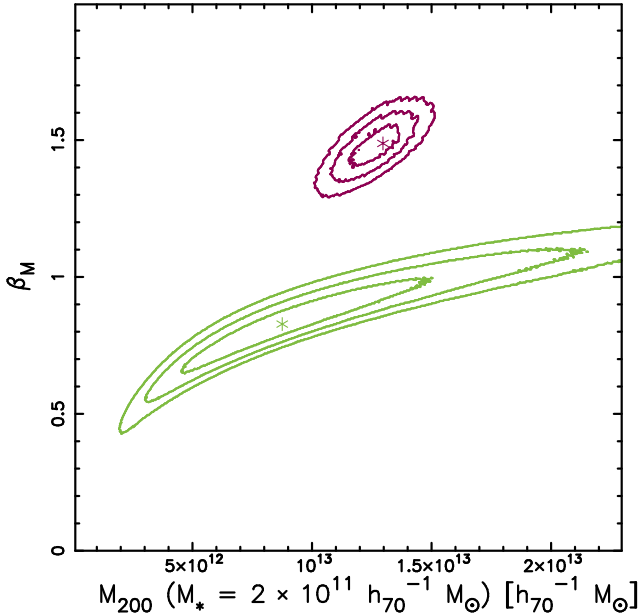


Figure 11. Constraints on the power law fits shown in Figure 10. In dark purple (light green) we show the constraints on the fit for red (blue) lenses, with lines representing the 67.8%, 95.4% and 99.7% confidence limits and stars representing the best-fit value.

fraction is difficult to constrain for high masses due to the shape of the halo model satellite terms. We therefore apply the same uniform satellite fraction prior to the high-stellar mass bins as we did to the high-luminosity bins, allowing a maximum α of 20%. The overall low satellite fraction for blue galaxies, suggesting together with low large-scale signal that most blue galaxies are isolated, is consistent with the luminosity results.

It is clear that the relation between dark matter halo and stellar mass is different for red and blue lenses. To quantify the difference, we fit a power law to the lensing signals in each bin simultaneously, similarly to our treatment of the luminosity bins in the previous section. The form of the power law is

$$M_{200} = M_{0,M} \left(\frac{M_*}{M_{\text{fid}}} \right)^{\beta_M} \quad (11)$$

with $M_{\text{fid}} = 2 \times 10^{11} h_{70}^{-2} M_{\odot}$ a scaling factor chosen to be the stellar mass of a fiducial galaxy as in VU11. We note that for the lowest red stellar mass bins, though the halo model fits the data very well (see Figure 9), the sample consists of nearly 100% satellite galaxies as mentioned above. The central halo mass associated with these lenses is therefore effectively inferred from the satellite term, and thus constrained indirectly by the halo model and so we exclude the two lowest stellar mass bins from our analysis.

The resulting best-fit values for red lenses are $M_{0,M} = 1.30^{+0.05}_{-0.09} \times 10^{13} h_{70}^{-1} M_{\odot}$ and $\beta_M = 1.49^{+0.06}_{-0.04}$, and for blue lenses $M_{0,M} = 0.88 \pm 0.13 \times 10^{13} h_{70}^{-1} M_{\odot}$ and $\beta_M = 0.83^{+0.05}_{-0.04}$. We show the constraints and best-fit values in Figure 11. The red lenses are clearly better constrained than the blue ones due to the stronger signal generated by these generally more massive galaxies. We note here that due to a lack of massive blue lenses in our analysis, the two galaxy type results probe different stellar mass ranges. The blue relation is limited to the low-stellar mass end only, while the red relation is constrained mostly at higher stellar masses.

The baryon fraction, M_*/M_{200} , is fairly constant between stellar mass bins though it shows a tendency to decrease for red lenses from $0.055^{+0.016}_{-0.015}$, for S3 to $0.008^{+0.002}_{-0.001}$, for S7. For blue lenses it conversely shows a slight increase from $0.009^{+0.005}_{-0.004}$, for S1 to $0.014^{+0.002}_{-0.001}$, for S4. These numbers are indicators of the baryon conversion efficiency, though the particular environment each sample resides in affects the numbers. Since the red and blue samples probe different stellar mass ranges, we cannot directly compare the two.

6 COMPARISON WITH PREVIOUS RESULTS

Early galaxy-galaxy lensing based works that have investigated the relation between luminosity and the virial mass of galaxies include Guzik & Seljak (2002) and Hoekstra et al. (2005). In these works, the mass is found to scale with luminosity as $\propto L^{1.4 \pm 0.2}$ and $\propto L^{1.6 \pm 0.2}$, respectively, in agreement with our findings. We focus, however, on comparing our halo mass results with those from three recent comprehensive galaxy-galaxy lensing halo model analyses which used data from three decidedly different surveys: the very wide but shallow SDSS (Mandelbaum et al. 2006), the moderately deep and wide RCS2 (VU11) and the very deep but narrow COSMOS (Leauthaud et al. 2012). All four datasets are shown in Figures 12 and 13, with our results denoted by solid dots.

We begin our comparison by noting that the various works employ different galaxy type separation criteria. Mandelbaum et al. (2006) and VU11 base their selection on the brightness profile of the lenses, while we use the SED type. As both selection criteria are found to correlate well with the colours of the lenses, we expect the galaxy samples to be similar — but not identical — and the differences between the samples could have some effect. Leauthaud et al. (2012) did not split their sample in red and blue, which is why we show the same constraints in both panels of Figures 12 and 13. Further variations between the anal-

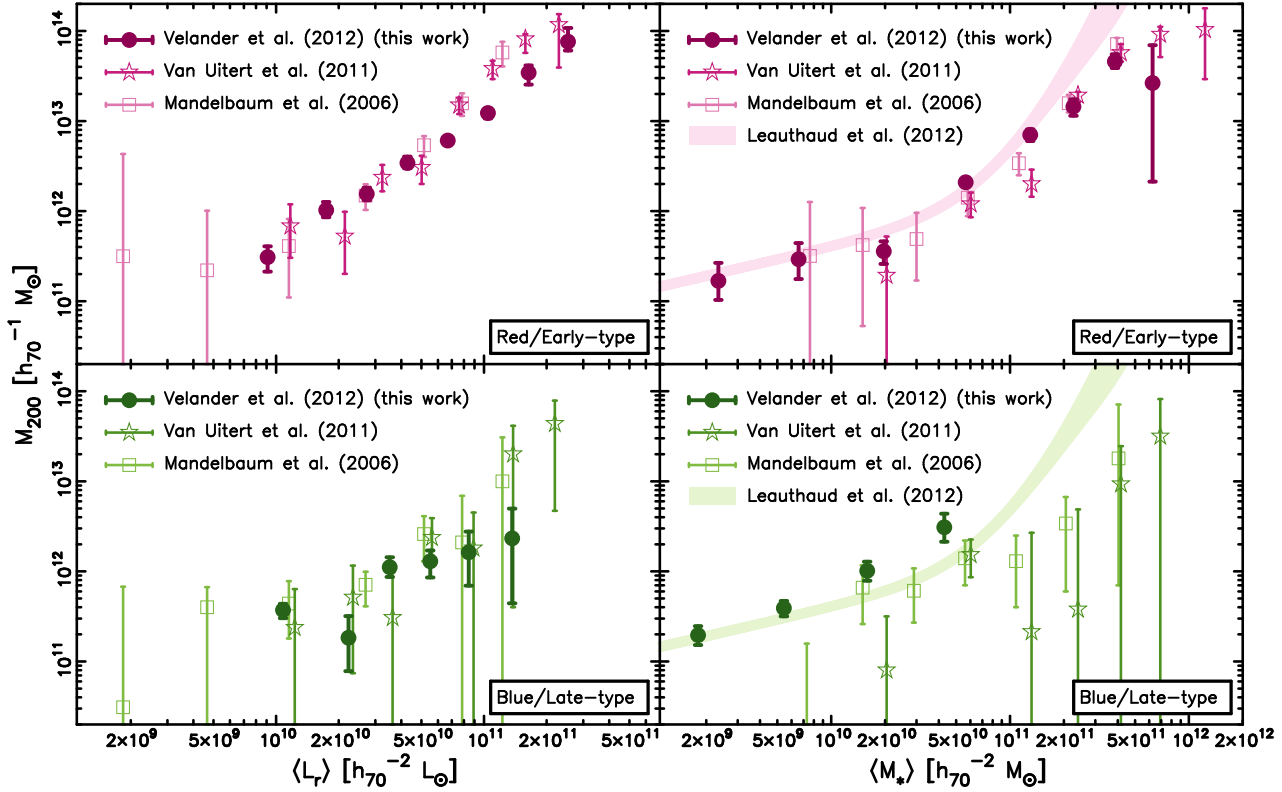


Figure 12. Comparison between four different datasets. The left (right) panels show the measured halo mass as a function of luminosity (stellar mass), and the top (bottom) panels show the results for red/early-type (blue/late-type) galaxies. The datasets used are all based on galaxy-galaxy lensing analyses with solid dots showing the CFHTLenS results from this paper. Also shown are halo masses measured using the RCS2 (open stars; VU11), the SDSS (open squares; Mandelbaum et al. 2006) and COSMOS (solid band; Leauthaud et al. 2012). In the case of COSMOS we use the results from their lowest redshift bin. Also note that no distinction between red and blue lenses was made in the COSMOS analysis, so the same results are shown in both right panels.

yses are discussed in more detail below. With these caveats in mind, we observe that all studies find similar general trends, with a halo mass that increases with increasing luminosity and/or stellar mass. It is also clear that blue/late-type galaxies tend to reside in haloes of lower mass than red/early-types do. The halo mass estimates of blue galaxies presented in these studies are in excellent agreement. For the red galaxies, our mass estimates are consistent with those from VU11 and Mandelbaum et al. (2006) except near $L_r \sim 10^{11} h_{70}^{-2} L_\odot$, where they are $2\text{--}3\sigma$ lower. However, as a function of stellar mass, our mass estimates of early-types broadly agree with theirs. The halo masses of early-types also agree with the results from Leauthaud et al. (2012) at stellar masses below $M_* \sim 10^{11} h_{70}^{-2} M_\odot$. At higher stellar masses, the mass estimates are $\sim 2\sigma$ lower than those from Leauthaud et al. (2012), but we note that this is also the case for the halo masses from VU11 and Mandelbaum et al. (2006). We will discuss this in more detail below. In general, a consistent picture of the relation between the baryonic properties of galaxies and their parent haloes is emerging from the four independent studies.

Since our halo model is most closely related to that used by VU11 (shown as open stars in Figures 12 and 13), a detailed comparison is more straight-forward compared to the other analyses. In VU11, 1.7×10^4 lens galaxies were studied using the overlap between the SDSS and the RCS2. The combination of the two surveys allowed for accurate baryonic property estimates using the spectroscopic information from the SDSS, and a high source number density of 6.3 arcmin^{-2} owing to the greater depth and better observing conditions of the RCS2 compared to the SDSS. Because

we use photometric redshifts for our analysis our lens sample is more than sixty times that of VU11, reflecting the small fraction of galaxies that have spectroscopic redshifts determined by SDSS. The even greater depth of the CFHTLenS compared to the RCS2 means that our source density is a factor of 1.7 higher. Furthermore, in contrast to VU11 we have individual redshift estimates available for all our sources. The increased number density and redshift resolution in our analysis results in significantly tighter constraints on the relations between halo mass and luminosity, and between halo mass and stellar mass.

As evidenced by Figure 12, our halo masses agree well with those found by VU11 in general, though our halo mass relations are shallower; for red lenses we measure a power law slope for the relation between halo mass and luminosity of $1.56^{+0.04}_{-0.06}$, and between halo mass and stellar mass of $1.49^{+0.06}_{-0.04}$, while VU11 find slopes of $2.34^{+0.09}_{-0.16}$, and 1.9 ± 0.1 , respectively, using the same power law definitions. The general trend with stellar mass of a decreasing baryon conversion efficiency for red lenses was observed by VU11 as well, but they were unable to discern a trend in their late-type sample. There are some differences between the analyses which should be noted, however. As mentioned above, we divide our lens sample in a red and blue one based on the SED type, while VU11 use the brightness distribution profiles to separate their lenses in a bulge-dominated and a disk-dominated sample. Even though the resulting samples are expected to be fairly similar, they are not identical. As the mass-to-luminosity ratio of galaxies strongly depends on their colour, even small colour differences between the samples could result in different masses. This may explain why our

halo mass estimates of the red lenses at the high luminosity end are lower than those of VU11 and Mandelbaum et al. (2006), who both use identical galaxy type separation criteria and whose masses agree in this regime. The difference is smaller for the stellar mass results, providing further support for this hypothesis.

Furthermore, in our halo model we account for the baryonic mass of each lens, something that was not done in VU11. Removing the baryonic component from our model, we find that the masses for some bins increase by as much as 15%. It may appear counter-intuitive that including a baryonic component with a mass which is of order 5% of the total mass should result in such a significantly lowered halo mass estimate. The explanation lies in the halo model fitting, and specifically in the way the satellite fraction is allowed to vary. Adding a baryonic component on small scales will result in a lowered central halo mass. The central halo profile reaches further than the baryonic component however, and thus power on intermediate scales is also diminished. To compensate for this loss of power, the halo model will increase the satellite 1-halo term by increasing the satellite fraction, which also increases the stripped satellite halo term, lowering the central 1-halo term further until an equilibrium is reached. These mechanisms are illustrated for red galaxies in luminosity bin L4 in Figure 14, where we have allowed halo mass, satellite fraction and stellar mass fraction to vary simultaneously for both panels. This figure also makes clear the degeneracies introduced to the halo model if the stellar mass is left as a free parameter in addition to halo mass and satellite fraction. Higher luminosity or stellar mass bins are more severely affected by this effect than the lower end due to the lack of a prominent satellite 1-halo feature. To study the effect on the best-fit power law parameters, we re-fit the halo models excluding the baryonic component. The resulting slope and amplitude of the power law do not change significantly. Hence this does not explain why VU11 find a steeper slope than we do. We note, however, that our baryonic component only accounts for the stars in the lens and not for example the hot gas. The influence of feedback on the gas distribution in galaxies is a complicated issue which may also affect our results, as discussed in van Daalen et al. (2011) and Semboloni et al. (2011), but it is an effect which we do not attempt to model here. However, as future lensing surveys grow more powerful and the data allows for greater accuracy this will be an important effect to study.

Another factor to take into account is the fact that we limit our lens samples to redshifts of $0.2 \leq z_{\text{lens}} \leq 0.4$ keeping our mean lens redshift fairly stable at $\langle z_{\text{lens}} \rangle \sim 0.3$. This is not done in VU11, and as a result the median redshift of our lower luminosity or stellar mass bins is higher than for the same bins in VU11, with the opposite being true for the higher bins. Recent numerical simulations indicate that the relation between stellar mass and halo mass will evolve with redshift (see for example Conroy & Wechsler 2009; Moster et al. 2010). Lower-mass host galaxies ($M_* < 10^{11} M_\odot$) increase in stellar mass faster than their halo mass increases, i.e. for higher redshifts the halo mass is lower for the same stellar mass. The opposite trend holds for higher-mass host galaxies ($M_* > 10^{11} M_\odot$). As a result, the relation between halo mass and stellar mass (or an indicator thereof, such as luminosity) steepens with increasing redshift. This means that for the lower-luminosity bins, where our redshifts are higher, we may measure a steeper slope than VU11 and vice-versa for higher-luminosity bins. The effect is likely small, however, because of the relatively small redshift ranges involved.

Finally we note that the lenses in the sample studied by VU11 are rather massive and luminous as only galaxies with spectroscopy are used. Our lens sample includes many more low luminosity and

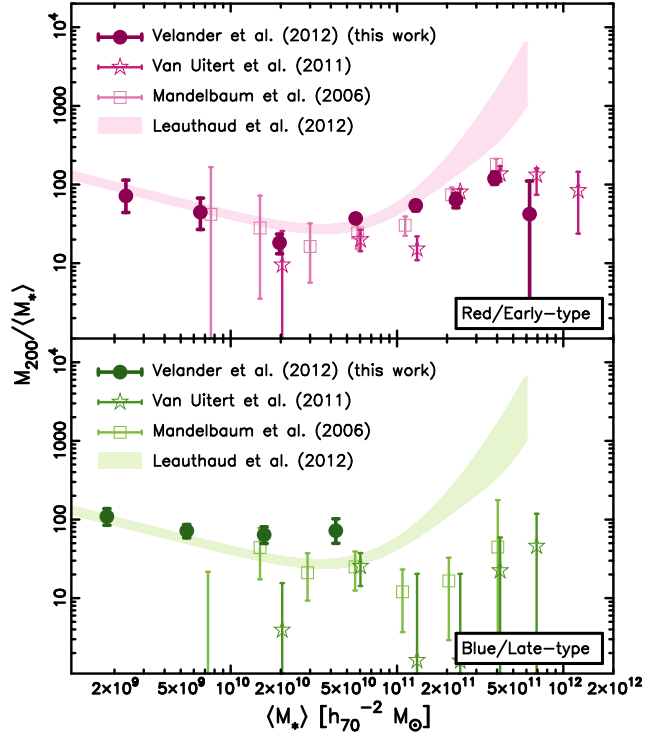


Figure 13. Comparison between four different datasets, showing the ratio of measured halo mass to stellar mass as a function of stellar mass. The top (bottom) panels show the results for red/early-type (blue/late-type) galaxies. The datasets used are all based on galaxy-galaxy lensing analyses with solid dots showing the CFHTLenS results from this paper. Also shown are halo masses measured using the RCS2 (open stars; VU11), the SDSS (open squares Mandelbaum et al. 2006) and COSMOS (solid band; Leauthaud et al. 2012). In the case of COSMOS we use the results from their lowest redshift bin. Also note that no distinction between red and blue lenses was made in the COSMOS analysis, so the same results are shown in both panels.

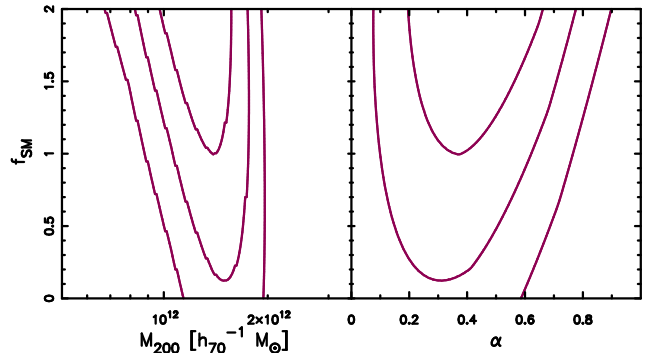


Figure 14. Dependence of halo model fitting parameters halo mass M_{200} and satellite fraction α on stellar mass, with f_{SM} the fraction of true mean stellar mass used in the halo model and contours showing the 67.8%, 95.4% and 99.7% confidence intervals. The left panel shows that including a baryonic component in the model (i.e. setting $f_{\text{SM}} = 1$) will result in a significantly lower best-fit halo mass than not doing so ($f_{\text{SM}} = 0$), and the right panel shows that the reason for this is an increased satellite fraction. In our analysis we keep the stellar mass component fixed at $f_{\text{SM}} = 1$.

low stellar mass objects, however. Hence the difference in slope may be partly due to the fact that we probe different regimes, and that the relation between baryonic observable and halo mass is not simply a power law but turns upward at high luminosities/stellar masses, as the results from Leauthaud et al. (2012) suggest.

Having compared our analysis to that of VU11, we now turn our attention to the comparison with the Mandelbaum et al. (2006) analysis of 3.5×10^5 lenses in the SDSS DR7, shown as open squares in Figures 12 and 13. Their lens sample is, similarly to the VU11 sample, also divided into early- and late-type galaxies based on their brightness profiles. To allow for a comparison between our results and theirs we first have to consider the differences in the luminosity definition. Mandelbaum et al. (2006) use absolute magnitudes which are based on a K correction to a redshift of $z = 0.1$ and a distance modulus calculated using $h = 1.0$. Furthermore, their luminosities are corrected for passive evolution by applying a factor $1.6(z - 0.1)$. However, VU11 convert their luminosities, which are similar to ours, using the Mandelbaum et al. (2006) definition and find that for low-luminosity low-redshift samples the difference between the two definitions is negligible. The more luminous lenses reside at higher redshifts and for them the correction is found to be greater, most likely due to the difference in the passive evolution corrections. Since our lenses are confined to relatively low redshifts, and since the main difference between luminosity definitions is the passive evolution factor, we can compare our results to Mandelbaum et al. (2006) without correcting the luminosities. Our halo mass definition is also different to that used by Mandelbaum et al. (2006) though. Mandelbaum et al. (2006) define the mass within the radius where the density is 180 times the mean background density while we set it to be 200 times the critical density. The correction factor stemming from the different definitions amounts to $\sim 30\%$. Having corrected for this, our results are then very similar to those from Mandelbaum et al. (2006), but the same concerns of object selection and baryonic contribution discussed above apply here as well. The relation that Mandelbaum et al. (2006) find between halo mass and luminosity for red lenses is shallower than the one found by VU11, as discussed therein, and are therefore more in agreement with our results. For the stellar mass relation, however, they find a steeper power law slope, though this result is mostly driven by their highest stellar mass bin as pointed out by VU11.

Finally, Leauthaud et al. (2012) perform a combined analysis of galaxy-galaxy lensing, galaxy clustering and galaxy number densities using data from the COSMOS survey, shown as a solid band in the right panels of Figure 12 and in Figure 13. For our comparison we select the results from their lowest redshift bin, since its redshift range of $0.22 < z < 0.48$ is very similar to the redshift range used here. Contrary to the other datasets, Leauthaud et al. (2012) did not separate their lens sample according to galaxy type. The results shown in the top panel of Figures 12 and 13 are therefore identical to those shown in the bottom panel. Note that at high stellar masses, their sample is expected to be dominated by red galaxies, and at low stellar masses by blue galaxies, as these are generally more abundant in the respective regimes (see Table 3). For stellar masses lower than $10^{11} h_{70}^{-1} M_*$, the agreement between Leauthaud et al. (2012) and the other galaxy-galaxy lensing results is excellent for both galaxy types. For higher stellar masses, however, Leauthaud et al. (2012) find higher halo masses than what has been observed in the lensing only analyses discussed above. This may be explained if a larger fraction of the galaxies used in the Leauthaud et al. (2012) analysis reside in dense environments and can be associated with galaxy groups and clusters such that

their halo masses correspond to the total mass of these structures. This theory is corroborated by Figure 10 of Leauthaud et al. (2012) which shows that for large stellar masses, the ratio of stellar mass to halo mass is very similar to that determined for a set of X-ray luminous clusters in Hoekstra (2007), indicating that we are entering the cluster regime. Furthermore, the sampling variance is not taken into account in the COSMOS error range. This is likely to affect the higher stellar mass bins more because the number of objects there is sparse. Additionally, the results from the COSMOS analysis of X-ray selected groups presented in Leauthaud et al. (2010), which is centred on a redshift similar to ours and also shown in Figure 10 of Leauthaud et al. (2012) as grey squares, agree better with our results for higher stellar masses. We note, however, that another possibility is that the high stellar mass end constraints from Leauthaud et al. (2012) may be driven mainly by the stellar mass function rather than by the lensing measurements. This, combined with the differences in the two halo model implementations, could also contribute to the observed discrepancy.

A further subtlety discussed in Section 4.2 is that the satellite fraction of galaxies with high stellar masses is not well constrained by galaxy-galaxy lensing only. Since the satellite fraction and halo mass are weakly anti-correlated (see VU11), our halo masses may be slightly underestimated if the satellite fractions are too high. Furthermore, the modelling of the shear signal from satellites in this mass range is a bit uncertain as they may have been stripped of more than the 50% of their dark matter we have assumed so far, and this could also have some effect. However, we estimate that these modelling uncertainties only have a small effect on our best-fit halo masses, and that it is not sufficient to explain the differences between the results.

7 CONCLUSION

In this work we have used high-quality weak lensing data produced by the CFHTLenS collaboration to place galaxy-galaxy lensing constraints on the relation between dark matter halo mass and the baryonic content of the lenses, quantified through luminosity and stellar mass estimates. The combination of large area and high source number density in this survey has made it possible to achieve tighter constraints compared to previous lensing surveys such as the SDSS, COSMOS or the RCS2. We also extended our study to lower stellar masses than have been studied before using a halo model such as the one described here.

In this paper we have included a halo model constituent which was neglected by most earlier implementations: the baryonic component. Since the lensing signal is a response to the total mass of a system, it is essential to account for baryons in order to not overestimate the mass contained in the dark matter halo. We have shown, however, that care has to be taken when including a baryonic component since doing so has a greater impact on the fitted halo mass than one might naively expect due to the complicated interplay between stellar mass, satellite fraction and halo mass.

As luminosity and stellar mass increases, the halo mass increases as well. For red lenses, the halo mass increases with greater baryonic content at a higher rate than for blue galaxies, independent of whether the measure of baryonic content is luminosity or stellar mass. The two measures thus produce comparable results. For each we fit power law relations to quantify the rate of increase in halo mass. We find a best-fit slope of $1.56_{-0.06}^{+0.04}$ and a normalisation of $1.26_{-0.06}^{+0.07} \times 10^{13} h_{70}^{-1} M_\odot$ for a fiducial luminosity of $L_{\text{fid}} = 10^{11} h_{70}^{-2} L_\odot$ for red galax-

ies, while for blue galaxies we find a slope of $0.73^{+0.09}_{-0.08}$ and a normalisation $0.16 \pm 0.03 \times 10^{13} h_{70}^{-1} M_{\odot}$. The power law relation between stellar mass and halo mass has a slope of $1.49^{+0.06}_{-0.04}$ and a normalisation of $1.30^{+0.05}_{-0.09} \times 10^{13} h_{70}^{-1} M_{\odot}$ for a fiducial mass of $M_{\text{fid}} = 2 \times 10^{11} h_{70}^{-2} M_{\odot}$ for red galaxies, and for blue galaxies we find a slope of $0.83^{+0.05}_{-0.04}$ and a normalisation of $0.88 \pm 0.13 \times 10^{13} h_{70}^{-1} M_{\odot}$.

For our blue galaxy selection, the satellite fraction is low across all luminosities and stellar masses considered here. The signal at large scales for these samples is also generally low in the lowest luminosity and stellar mass bins, indicating that these galaxies are relatively isolated and reside in less clustered environments than the red galaxies do and that we may be overestimating the galaxy bias for these samples. At low luminosity/stellar mass, a considerable fraction of red galaxies are satellites within a larger dark matter halo. This fraction decreases steadily with increasing luminosity or stellar mass. In general, the satellite fractions show that at these redshifts the galaxies in denser regions are mostly red while for the same luminosity or stellar mass isolated galaxies tend to be bluer and thus star forming. This indicates that the star formation history of galaxies differs depending on the density of the environment they are residing in. Furthermore, since blue galaxies have a fairly shallow relation between halo mass and baryonic mass there are a range of stellar masses possible for a given halo mass. This is not true for red galaxies, which therefore have a narrower range of baryon conversion efficiencies for a given halo mass than blue galaxies.

Another finding of this work is that for faint and low stellar mass blue galaxies, the amplitude of the lensing signal at projected separations larger than $\sim 2h_{70}^{-1} \text{Mpc}$ is lower than the corresponding best-fit halo model. For the red galaxies, the halo model fits the data well over all scales. This could indicate that while the bias description works well for red galaxies, it is not optimal for blue galaxies. If this is the case, then the environments in which the two samples reside are radically different and the difference will have to be taken into account in the future. Alternatively, the discrepancy could be caused by other choices that affect the 1-halo to 2-halo transition regime in our halo model implementation. Currently, we do not have enough data to favour or rule out either scenario, but we plan to explore this further in upcoming works.

The relations between baryonic content indicators and dark matter halo mass presented in this work, as well as the dependence of the satellite fraction on luminosity and stellar mass, improve our understanding of the mechanisms behind galaxy formation since they provide constraints that can be directly compared to numerical simulations that model different galaxy formation scenarios. With currently ongoing (for instance DES⁴ or KiDS; de Jong et al. 2013) and planned (such as LSST⁵, HSC⁶ or Euclid⁷; Laureijs et al. 2011) surveys, weak lensing analyses will become yet more powerful than the one presented in this paper. In preparation for the future there are therefore several sources of uncertainty that should be investigated. As mentioned above, the galaxy bias description may not be optimal for blue lenses and with future data this bias can likely be constrained directly using galaxy-galaxy lensing observations. Recent simulations have also indicated that there is a redshift evolution of the halo mass relations, and this evolution can be stud-

ied with weak lensing (see Choi et al. 2012; Hudson et al. 2013). Other possible improvements to the halo model used here include studies of the distribution of satellites within a galaxy dark matter halo, a more accurate description of the regime where the 1-halo term and 2-halo term overlap (i.e. halo exclusion), and investigations into the stripping of satellite haloes. The analysis presented in this paper is a significant advance on recent analyses, and with future surveys we will be able to use galaxy-galaxy lensing to study the connection between baryons and dark matter in exquisite detail.

ACKNOWLEDGMENTS

We thank R. Bielby, O. Ilbert and the TERAPIX team for making the WIRDS stellar mass catalogue available to us, and Peter Schneider for valuable comments on the manuscript. Additionally, we thank the anonymous referee for their insightful comments which helped improve this paper and ensure its robustness.

This work is based on observations obtained with MegaPrime/MegaCam, a joint project of CFHT and CEA/DAPNIA, at the Canada-France-Hawaii Telescope (CFHT) which is operated by the National Research Council (NRC) of Canada, the Institut National des Sciences de l’Univers of the Centre National de la Recherche Scientifique (CNRS) of France, and the University of Hawaii. This research used the facilities of the Canadian Astronomy Data Centre operated by the National Research Council of Canada with the support of the Canadian Space Agency. We thank the CFHT staff for successfully conducting the CFHTLS observations and in particular Jean-Charles Cuillandre and Eugene Magnier for the continuous improvement of the instrument calibration and the Elixir detrended data that we used. We also thank TERAPIX for the quality assessment and validation of individual exposures during the CFHTLS data acquisition period, and Emmanuel Bertin for developing some of the software used in this study. CFHTLenS data processing was made possible thanks to significant computing support from the NSERC Research Tools and Instruments grant program, and to HPC specialist Ovidiu Toader. The early stages of the CFHTLenS project was made possible thanks to the support of the European Commission’s Marie Curie Research Training Network DUEL (MRTN-CT-2006-036133) which directly supported six members of the CFHTLenS team (LF, HH, PS, BR, CB, MV) between 2007 and 2011 in addition to providing travel support and expenses for team meetings.

MV acknowledges support from the European DUEL Research-Training Network (MRTN-CT-2006-036133), from the Netherlands Organization for Scientific Research (NWO) and from the Beecroft Institute for Particle Astrophysics and Cosmology. H. Hoekstra acknowledges support from Marie Curie IRG grant 230924, the Netherlands Organisation for Scientific Research (NWO) grant number 639.042.814 and from the European Research Council under the EC FP7 grant number 279396. TE is supported by the Deutsche Forschungsgemeinschaft through project ER 327/3-1 and the Transregional Collaborative Research Centre TR 33 - “The Dark Universe”. CH acknowledges support from the European Research Council under the EC FP7 grant number 240185. H. Hildebrandt is supported by the Marie Curie IOF 252760, a CITA National Fellowship, and the DFG grant Hi 1495/2-1. TDK acknowledges support from a Royal Society University Research Fellowship. YM acknowledges support from CNRS/INSU (Institut National des Sciences de l’Univers) and the Programme National Galaxies et Cosmologie (PNCG). LVW ac-

⁴ www.darkenergysurvey.org

⁵ www.lsst.org

⁶ www.subarutelescope.org/Projects/HSC

⁷ www.euclid-ec.org

knowledge support from the Natural Sciences and Engineering Research Council of Canada (NSERC) and the Canadian Institute for Advanced Research (CIFAR, Cosmology and Gravity program). LF acknowledges support from NSFC grants 11103012 & 10878003, Innovation Program 12ZZ134 and Chen Guang project 10CG46 of SMEC, and STCSM grant 11290706600 & Pujiang Program 12PJ1406700. SG acknowledges support from the Netherlands Organization for Scientific Research (NWO) through VIDI grant 639.042.814. MJH acknowledges support from the Natural Sciences and Engineering Research Council of Canada (NSERC). BR acknowledges support from the European Research Council in the form of a Starting Grant with number 24067. TS acknowledges support from NSF through grant AST-0444059-001, SAO through grant GO0-11147A, and NWO. ES acknowledges support from the Netherlands Organisation for Scientific Research (NWO) grant number 639.042.814 and support from the European Research Council under the EC FP7 grant number 279396.

Author Contributions: All authors contributed to the development and writing of this paper. The authorship list reflects the lead authors of this paper (MV, EvU and H. Hoekstra) followed by two alphabetical groups. The first alphabetical group includes key contributors to the science analysis and interpretation in this paper, the founding core team and those whose long-term significant effort produced the final CFHTLenS data product. The second group covers members of the CFHTLenS team who made a significant contribution to the project and/or this paper. The CFHTLenS collaboration was co-led by CH and LVW and the CFHTLenS Galaxy-Galaxy Lensing Working Group was led by BR and CB.

REFERENCES

- Adelman-McCarthy J. K., Agüeros M. A., Allam S. S., Anderson K. S. J., Anderson S. F., Annis J., Bahcall N. A., Baldry I. K., Barentine J. C., Berlind A., Bernardi M., Blanton M. R., Boroski W. N., Brewington H. J., Brinchmann J., Brinkmann J., Brunner R. J., Budavári T., Carey L. N., Carr M. A., Castander F. J., Connolly A. J., Csabai I., Czarapata P. C., Dalcanton J. J., Doi M., Dong F., Eisenstein D. J., Evans M. L., Fan X., Finkbeiner D. P., Friedman S. D., Frieman J. A., Fukugita M., Gillespie B., Glazebrook K., Gray J., Grebel E. K., Gunn J. E., Gurbani V. K., de Haas E., Hall P. B., Harris F. H., Harvanek M., Hawley S. L., Hayes J., Hendry J. S., Hennessy G. S., Hindsley R. B., Hirata C. M., Hogan C. J., Hogg D. W., Holmgren D. J., Holtzman J. A., Ichikawa S.-i., Ivezić Ž., Jester S., Johnston D. E., Jorgensen A. M., Jurić M., Kent S. M., Kleinman S. J., Knapp G. R., Kniazev A. Y., Kron R. G., Krzesinski J., Kuropatkin N., Lamb D. Q., Lampeitl H., Lee B. C., Leger R. F., Lin H., Long D. C., Loveday J., Lupton R. H., Margon B., Martínez-Delgado D., Mandelbaum R., Matsubara T., McGehee P. M., McKay T. A., Meiksin A., Munn J. A., Nakajima R., Nash T., Neilsen Jr. E. H., Newberg H. J., Newman P. R., Nichol R. C., Nicinski T., Nieto-Santisteban M., Nitta A., O’Mullane W., Okamura S., Owen R., Padmanabhan N., Pauls G., Peoples Jr. J., Pier J. R., Pope A. C., Pourbaix D., Quinn T. R., Richards G. T., Richmond M. W., Rockosi C. M., Schlegel D. J., Schneider D. P., Schroeder J., Scranton R., Seljak U., Sheldon E., Shimasaku K., Smith J. A., Smolčić V., Snedden S. A., Stoughton C., Strauss M. A., SubbaRao M., Szalay A. S., Szapudi I., Szkody P., Tegmark M., Thakar A. R., Tucker D. L., Uomoto A., Vanden Berk D. E., Vandenberg J., Vogeley M. S., Voges W., Vogt N. P., Walkowicz L. M., Weinberg D. H., West A. A., White S. D. M., Xu Y., Yanny B., Yocum D. R., York D. G., Zehavi I., Zibetti S., Zucker D. B., 2006, *ApJS*, 162, 38
- Arnouts S., Cristiani S., Moscardini L., Matarrese S., Lucchin F., Fontana A., Giallongo E., 1999, *MNRAS*, 310, 540
- Arnouts S., Walcher C. J., Le Fèvre O., Zamorani G., Ilbert O., Le Brun V., Pozzetti L., Bardelli S., Tresse L., Zucca E., Charlot S., Lamareille F., McCracken H. J., Bolzonella M., Iovino A., Lonsdale C., Polletta M., Surace J., Bottini D., Garilli B., Maccagni D., Picat J. P., Scaramella R., Scodeggio M., Vettolani G., Zanichelli A., Adami C., Cappi A., Ciliegi P., Contini T., de la Torre S., Foucaud S., Franzetti P., Gavignaud I., Guzzo L., Marano B., Marinoni C., Mazure A., Meneux B., Merighi R., Paltani S., Pellò R., Pollo A., Radovich M., Tempurin S., Vergani D., 2007, *A&A*, 476, 137
- Bell E. F., 2008, *ApJ*, 682, 355
- Bell E. F., de Jong R. S., 2001, *ApJ*, 550, 212
- Benítez N., 2000, *ApJ*, 536, 571
- Bielby R., Hudelot P., McCracken H. J., Ilbert O., Daddi E., Le Fèvre O., Gonzalez-Perez V., Kneib J.-P., Marmo C., Mellier Y., Salvato M., Sanders D. B., Willott C. J., 2012, *A&A*, 545, A23
- Borch A., Meisenheimer K., Bell E. F., Rix H.-W., Wolf C., Dye S., Kleinheinrich M., Kovacs Z., Wisotzki L., 2006, *A&A*, 453, 869
- Brainerd T. G., Blandford R. D., Smail I., 1996, *ApJ*, 466, 623
- Bruzual G., Charlot S., 2003, *MNRAS*, 344, 1000
- Calzetti D., Armus L., Bohlin R. C., Kinney A. L., Koornneef J., Storchi-Bergmann T., 2000, *ApJ*, 533, 682
- Chabrier G., 2003, *PASP*, 115, 763
- Choi A., Tyson J. A., Morrison C. B., Jee M. J., Schmidt S. J., Margoniner V. E., Wittman D. M., 2012, *ApJ*, 759, 101
- Coe D., Benítez N., Sánchez S. F., Jee M., Bouwens R., Ford H., 2006, *AJ*, 132, 926
- Coleman G. D., Wu C.-C., Weedman D. W., 1980, *ApJS*, 43, 393
- Conroy C., Wechsler R. H., 2009, *ApJ*, 696, 620
- Cooray A., Sheth R., 2002, *Phys. Rep.*, 372, 1
- Coupon J., Kilbinger M., McCracken H. J., Ilbert O., Arnouts S., Mellier Y., Abbas U., de la Torre S., Goranova Y., Hudelot P., Kneib J.-P., Le Fèvre O., 2012, *A&A*, 542, A5
- Davis M., Faber S. M., Newman J., Phillips A. C., Ellis R. S., Steidel C. C., Conselice C., Coil A. L., Finkbeiner D. P., Koo D. C., Guhathakurta P., Weiner B., Schiavon R., Willmer C., Kaiser N., Luppino G. A., Wirth G., Connolly A., Eisenhardt P., Cooper M., Gerke B., 2003, *SPIE*, 4834, 161
- Davis M., Guhathakurta P., Konidaris N. P., Newman J. A., Ashby M. L. N., Biggs A. D., Barmby P., Bundy K., Chapman S. C., Coil A. L., Conselice C. J., Cooper M. C., Croton D. J., Eisenhardt P. R. M., Ellis R. S., Faber S. M., Fang T., Fazio G. G., Georgakakis A., Gerke B. F., Goss W. M., Gwyn S., Harker J., Hopkins A. M., Huang J.-S., Ivison R. J., Kassin S. A., Kirby E. N., Koekemoer A. M., Koo D. C., Laird E. S., Le Floc’h E., Lin L., Lotz J. M., Marshall P. J., Martin D. C., Metevier A. J., Moustakas L. A., Nandra K., Noeske K. G., Papovich C., Phillips A. C., Rich R. M., Rieke G. H., Rigopoulou D., Salim S., Schiminovich D., Simard L., Smail I., Small T. A., Weiner B. J., Willmer C. N. A., Willner S. P., Wilson G., Wright E. L., Yan R., 2007, *ApJL*, 660, L1
- de Jong J. T. A., Verdoes Kleijn G. A., Kuijken K. H., Valentijn E. A., 2013, *Experimental Astronomy*, 35, 25
- Duffy A. R., Schaye J., Kay S. T., Dalla Vecchia C., 2008, *MNRAS*, 390, L64
- Eddington A. S., 1913, *MNRAS*, 73, 359
- Eisenstein D. J., Annis J., Gunn J. E., Szalay A. S., Connolly A. J.,

- Nichol R. C., Bahcall N. A., Bernardi M., Burles S., Castander F. J., Fukugita M., Hogg D. W., Ivezić Ž., Knapp G. R., Lupton R. H., Narayanan V., Postman M., Reichart D. E., Richmond M., Schneider D. P., Schlegel D. J., Strauss M. A., SubbaRao M., Tucker D. L., Vanden Berk D., Vogeley M. S., Weinberg D. H., Yanny B., 2001, *AJ*, 122, 2267
- Erben T., Hildebrandt H., Lerchster M., Hudelot P., Benjamin J., van Waerbeke L., Schrabback T., Brimiouille F., Cordes O., Dietrich J. P., Holhjem K., Schirmer M., Schneider P., 2009, *A&A*, 493, 1197
- Erben T., Hildebrandt H., Miller L., van Waerbeke L., Heymans C., Hoekstra H., Kitching T. D., Mellier Y., Benjamin J., Blake C., Bonnett C., Cordes O., Coupon J., Fu L., Gavazzi R., Gillis B., Grocutt E., Gwyn S. D. J., Holhjem K., Hudson M. J., Kilbinger M., Kuijken K., Milkeraitis M., Rowe B. T. P., Schrabback T., Semboloni E., Simon P., Smit M., Toader O., Vafaei S., van Uitert E., Velander M., 2012, preprint (astro-ph/1210.8156)
- Gallazzi A., Charlot S., Brinchmann J., White S. D. M., Tremonti C. A., 2005, *MNRAS*, 362, 41
- Garilli B., Le Fèvre O., Guzzo L., Maccagni D., Le Brun V., de la Torre S., Meneux B., Tresse L., Franzetti P., Zamorani G., Zanichelli A., Gregorini L., Vergani D., Bottini D., Scaramella R., Scodreggio M., Vettolani G., Adami C., Arnouts S., Bardelli S., Bolzonella M., Cappi A., Charlot S., Ciliegi P., Contini T., Foucaud S., Gavignaud I., Ilbert O., Iovino A., Lamareille F., McCracken H. J., Marano B., Marinoni C., Mazure A., Merighi R., Paltani S., Pellò R., Pollo A., Pozzetti L., Radovich M., Zucca E., Blaizot J., Bongiorno A., Cucciati O., Mellier Y., Moreau C., Paiero L., 2008, *A&A*, 486, 683
- Gilbank D. G., Gladders M. D., Yee H. K. C., Hsieh B. C., 2011, *AJ*, 141, 94
- Gillis B. R., Hudson M. J., Erben T., Heymans C., Hildebrandt H., Hoekstra H., Kitching T. D., Mellier Y., Miller L., van Waerbeke L., Bonnett C., Coupon J., Fu L., Hilbert S., Rowe B. T. P., Schrabback T., Semboloni E., van Uitert E., Velander M., 2013, preprint (astro-ph/1301.7421)
- Guzik J., Seljak U., 2002, *MNRAS*, 335, 311
- Heymans C., Van Waerbeke L., Miller L., Erben T., Hildebrandt H., Hoekstra H., Kitching T. D., Mellier Y., Simon P., Bonnett C., Coupon J., Fu L., Harois Déraps J., Hudson M. J., Kilbinger M., Kuijken K., Rowe B., Schrabback T., Semboloni E., van Uitert E., Vafaei S., Velander M., 2012, *MNRAS*, 427, 146
- Hildebrandt H., Arnouts S., Capak P., Moustakas L. A., Wolf C., Abdalla F. B., Assef R. J., Banerji M., Benítez N., Brammer G. B., Budavári T., Carliles S., Coe D., Dahlen T., Feldmann R., Gerdes D., Gillis B., Ilbert O., Kotulla R., Lahav O., Li I. H., Miralles J.-M., Purger N., Schmidt S., Singal J., 2010, *A&A*, 523, A31
- Hildebrandt H., Erben T., Kuijken K., van Waerbeke L., Heymans C., Coupon J., Benjamin J., Bonnett C., Fu L., Hoekstra H., Kitching T. D., Mellier Y., Miller L., Velander M., Hudson M. J., Rowe B. T. P., Schrabback T., Semboloni E., Benítez N., 2012, *MNRAS*, 421, 2355
- Hoekstra H., 2007, *MNRAS*, 379, 317
- Hoekstra H., Franx M., Kuijken K., Squires G., 1998, *ApJ*, 504, 636
- Hoekstra H., Hsieh B. C., Yee H. K. C., Lin H., Gladders M. D., 2005, *ApJ*, 635, 73
- Hoekstra H., Yee H. K. C., Gladders M. D., 2004, *ApJ*, 606, 67
- Hudson M. J., CFHTLenS, et al., 2013, *CFHTLenS*, preprint
- Hudson M. J., Gwyn S. D. J., Dahle H., Kaiser N., 1998, *ApJ*, 503, 531
- Ilbert O., Arnouts S., McCracken H. J., Bolzonella M., Bertin E., Le Fèvre O., Mellier Y., Zamorani G., Pellò R., Iovino A., Tresse L., Le Brun V., Bottini D., Garilli B., Maccagni D., Picat J. P., Scaramella R., Scodreggio M., Vettolani G., Zanichelli A., Adami C., Bardelli S., Cappi A., Charlot S., Ciliegi P., Contini T., Cucciati O., Foucaud S., Franzetti P., Gavignaud I., Guzzo L., Marano B., Marinoni C., Mazure A., Meneux B., Merighi R., Paltani S., Pollo A., Pozzetti L., Radovich M., Zucca E., Bondi M., Bongiorno A., Busarello G., de La Torre S., Gregorini L., Lamareille F., Mathez G., Merluzzi P., Ripepi V., Rizzo D., Vergani D., 2006, *A&A*, 457, 841
- Ilbert O., Salvato M., Le Floc'h E., Aussel H., Capak P., McCracken H. J., Mobasher B., Kartaltepe J., Scoville N., Sanders D. B., Arnouts S., Bundy K., Cassata P., Kneib J.-P., Koekemoer A., Le Fèvre O., Lilly S., Surace J., Taniguchi Y., Tasca L., Thompson D., Tresse L., Zamojski M., Zamorani G., Zucca E., 2010, *ApJ*, 709, 644
- Kaiser N., Squires G., Broadhurst T., 1995, *ApJ*, 449, 460
- Kauffmann G., Heckman T. M., White S. D. M., Charlot S., Tremonti C., Brinchmann J., Bruzual G., Peng E. W., Seibert M., Bernardi M., Blanton M., Brinkmann J., Castander F., Csábai I., Fukugita M., Ivezić Z., Munn J. A., Nichol R. C., Padmanabhan N., Thakar A. R., Weinberg D. H., York D., 2003, *MNRAS*, 341, 33
- Kilbinger M., Fu L., Heymans C., Simpson F., Benjamin J., Erben T., Harois-Déraps J., Hoekstra H., Hildebrandt H., Kitching T. D., Mellier Y., Miller L., Van Waerbeke L., Benabed K., Bonnett C., Coupon J., Hudson M. J., Kuijken K., Rowe B., Schrabback T., Semboloni E., Vafaei S., Velander M., 2013, *MNRAS*, 430, 2200
- Komatsu E., Smith K. M., Dunkley J., Bennett C. L., Gold B., Hinshaw G., Jarosik N., Larson D., Nolte M. R., Page L., Spergel D. N., Halpern M., Hill R. S., Kogut A., Limon M., Meyer S. S., Odegard N., Tucker G. S., Weiland J. L., Wollack E., Wright E. L., 2011, *ApJS*, 192, 18
- Laureijs R., Amiaux J., Arduini S., Auguères J.-L., Brinchmann J., Cole R., Cropper M., Dabin C., Duvet L., Ealet A., et al., 2011, preprint (astro-ph/1110.3193)
- Le Fèvre O., Vettolani G., Garilli B., Tresse L., Bottini D., Le Brun V., Maccagni D., Picat J. P., Scaramella R., Scodreggio M., Zanichelli A., Adami C., Arnaboldi M., Arnouts S., Bardelli S., Bolzonella M., Cappi A., Charlot S., Ciliegi P., Contini T., Foucaud S., Franzetti P., Gavignaud I., Guzzo L., Ilbert O., Iovino A., McCracken H. J., Marano B., Marinoni C., Mathez G., Mazure A., Meneux B., Merighi R., Paltani S., Pellò R., Pollo A., Pozzetti L., Radovich M., Zamorani G., Zucca E., Bondi M., Bongiorno A., Busarello G., Lamareille F., Mellier Y., Merluzzi P., Ripepi V., Rizzo D., 2005, *A&A*, 439, 845
- Leauthaud A., Finoguenov A., Kneib J.-P., Taylor J. E., Massey R., Rhodes J., Ilbert O., Bundy K., Tinker J., George M. R., Capak P., Koekemoer A. M., Johnston D. E., Zhang Y.-Y., Cappelletti N., Ellis R. S., Elvis M., Giodini S., Heymans C., Le Fèvre O., Lilly S., McCracken H. J., Mellier Y., Réfrégier A., Salvato M., Scoville N., Smoot G., Tanaka M., Van Waerbeke L., Wolk M., 2010, *ApJ*, 709, 97
- Leauthaud A., Tinker J., Behroozi P. S., Busha M. T., Wechsler R. H., 2011, *ApJ*, 738, 45
- Leauthaud A., Tinker J., Bundy K., Behroozi P. S., Massey R., Rhodes J., George M. R., Kneib J.-P., Benson A., Wechsler R. H., Busha M. T., Capak P., Cortés M., Ilbert O., Koekemoer A. M., Le Fèvre O., Lilly S., McCracken H. J., Salvato M., Schrabback T., Scoville N., Smith T., Taylor J. E., 2012, *ApJ*, 744, 159

Mandelbaum R., Hirata C. M., Seljak U., Guzik J., Padmanabhan N., Blake C., Blanton M. R., Lupton R., Brinkmann J., 2005a, *MNRAS*, 361, 1287

Mandelbaum R., Seljak U., Kauffmann G., Hirata C. M., Brinkmann J., 2006, *MNRAS*, 368, 715

Mandelbaum R., Slosar A., Baldauf T., Seljak U., Hirata C. M., Nakajima R., Reyes R., Smith R. E., 2012, preprint (astro-ph/1207.1120)

Mandelbaum R., Tasitsiomi A., Seljak U., Kravtsov A. V., Wechsler R. H., 2005b, *MNRAS*, 362, 1451

Miller L., Heymans C., Kitching T. D., van Waerbeke L., Erben T., Hildebrandt H., Hoekstra H., Mellier Y., Rowe B. T. P., Coupon J., Dietrich J. P., Fu L., Harnois-Déraps J., Hudson M. J., Kilbinger M., Kuijken K., Schrabback T., Semboloni E., Vafaei S., Velander M., 2013, *MNRAS*, 429, 2858

More S., van den Bosch F. C., Cacciato M., Skibba R., Mo H. J., Yang X., 2011, *MNRAS*, 410, 210

Moster B. P., Somerville R. S., Maulbetsch C., van den Bosch F. C., Macciò A. V., Naab T., Oser L., 2010, *ApJ*, 710, 903

Navarro J. F., Frenk C. S., White S. D. M., 1996, *ApJ*, 462, 563

Newman J. A., Cooper M. C., Davis M., Faber S. M., Coil A. L., Guhathakurta P., Koo D. C., Phillips A. C., Conroy C., Dutton A. A., Finkbeiner D. P., Gerke B. F., Rosario D. J., Weiner B. J., Willmer C. N. A., Yan R., Harker J. J., Kassir S. A., Konidaris N. P., Lai K., Madgwick D. S., Noeske K. G., Wirth G. D., Connolly A. J., Kaiser N., Kirby E. N., Lemaux B. C., Lin L., Lotz J. M., Luppino G. A., Marinoni C., Matthews D. J., Metevier A., Schiavon R. P., 2012, preprint (astro-ph/1203.3192)

Parker L. C., Hoekstra H., Hudson M. J., van Waerbeke L., Mellier Y., 2007, *ApJ*, 669, 21

Paulin-Henriksson S., Amara A., Voigt L., Refregier A., Bridle S. L., 2008, *A&A*, 484, 67

Pozzetti L., Bolzonella M., Lamareille F., Zamorani G., Franzetti P., Le Fèvre O., Iovino A., Temporin S., Ilbert O., Arnouts S., Charlot S., Brinchmann J., Zucca E., Tresse L., Scodreggio M., Guzzo L., Bottini D., Garilli B., Le Brun V., Maccagni D., Picat J. P., Scaramella R., Vettolani G., Zanichelli A., Adami C., Bardelli S., Cappi A., Ciliegi P., Contini T., Foucaud S., Gavignaud I., McCracken H. J., Marano B., Marinoni C., Mazure A., Meneux B., Merighi R., Paltani S., Pellò R., Pollo A., Radovich M., Bondi M., Bongiorno A., Cucciati O., de la Torre S., Gregorini L., Mellier Y., Merluzzi P., Vergani D., Walcher C. J., 2007, *A&A*, 474, 443

Salim S., Rich R. M., Charlot S., Brinchmann J., Johnson B. D., Schiminovich D., Seibert M., Mallery R., Heckman T. M., Forster K., Friedman P. G., Martin D. C., Morrissey P., Neff S. G., Small T., Wyder T. K., Bianchi L., Donas J., Lee Y.-W., Madore B. F., Milliard B., Szalay A. S., Welsh B. Y., Yi S. K., 2007, *ApJS*, 173, 267

Schneider P., Rix H., 1997, *ApJ*, 474, 25

Scoville N., Abraham R. G., Aussel H., Barnes J. E., Benson A., Blain A. W., Calzetti D., Comastri A., Capak P., Carilli C., Carlstrom J. E., Carollo C. M., Colbert J., Daddi E., Ellis R. S., Elvis M., Ewald S. P., Fall M., Franceschini A., Giavalisco M., Green W., Griffiths R. E., Guzzo L., Hasinger G., Impey C., Kneib J., Koda J., Koekemoer A., Lefevre O., Lilly S., Liu C. T., McCracken H. J., Massey R., Mellier Y., Miyazaki S., Mobasher B., Mould J., Norman C., Refregier A., Renzini A., Rhodes J., Rich M., Sanders D. B., Schiminovich D., Schinnerer E., Scodreggio M., Sheth K., Shopbell P. L., Taniguchi Y., Tyson N. D., Urry C. M., Van Waerbeke L., Vettolani P., White S. D. M., Yan L., 2007, *ApJS*, 172, 38

Table A1. Redshift bias fit parameters for red and blue subsamples. The slope a is kept fixed between magnitude bins while the offset b is allowed to vary.

Magnitude bin	a_{red}	$b_{\text{red}} [\times 10^{-2}]$	a_{blue}	$b_{\text{blue}} [\times 10^{-2}]$
(14,19]	0.99	-0.62	1.08	-2.52
(19,20]	0.99	0.20	1.08	7.46
(20,21]	0.99	4.64	1.08	3.69
(21,22]	0.99	4.64	1.08	5.07
(22,23]	—	—	1.08	4.06

Semboloni E., Hoekstra H., Schaye J., van Daalen M. P., McCarthy I. G., 2011, *MNRAS*, 417, 2020

Sheldon E. S., Johnston D. E., Frieman J. A., Scranton R., McKay T. A., Connolly A. J., Budavári T., Zehavi I., Bahcall N. A., Brinkmann J., Fukugita M., 2004, *AJ*, 127, 2544

Sheth R. K., Mo H. J., Tormen G., 2001, *MNRAS*, 323, 1

Smith R. E., Peacock J. A., Jenkins A., White S. D. M., Frenk C. S., Pearce F. R., Thomas P. A., Efsthathiou G., Couchman H. M. P., 2003, *MNRAS*, 341, 1311

Strauss M. A., Weinberg D. H., Lupton R. H., Narayanan V. K., Annis J., Bernardi M., Blanton M., Burles S., Connolly A. J., Dalcanton J., Doi M., Eisenstein D., Frieman J. A., Fukugita M., Gunn J. E., Ivezić Ž., Kent S., Kim R. S. J., Knapp G. R., Kron R. G., Munn J. A., Newberg H. J., Nichol R. C., Okamura S., Quinn T. R., Richmond M. W., Schlegel D. J., Shimasaku K., SubbaRao M., Szalay A. S., Vanden Berk D., Vogeley M. S., Yanny B., Yasuda N., York D. G., Zehavi I., 2002, *AJ*, 124, 1810

Tinker J. L., George M. R., Leauthaud A., Bundy K., Finoguenov A., Massey R., Rhodes J., Wechsler R. H., 2012, *ApJL*, 755, L5

Tinker J. L., Weinberg D. H., Zheng Z., Zehavi I., 2005, *ApJ*, 631, 41

van Daalen M. P., Schaye J., Booth C. M., Dalla Vecchia C., 2011, *MNRAS*, 415, 3649

van Uitert E., Hoekstra H., Velander M., Gilbank D. G., Gladders M. D., Yee H. K. C., 2011, *A&A*, 534, A14+

Velander M., Kuijken K., Schrabback T., 2011, *MNRAS*, 412, 2665

APPENDIX A: CORRECTIONS FOR SIGNAL CONTAMINATION

A1 Photometric redshift bias correction

Though the quality of the CFHTLenS photometric redshift estimates is high, there is still a small bias present due to the inherent limitations of template-based Bayesian methods, as discussed in Hildebrandt et al. (2012). This bias will affect not only the redshift itself, but also the derived quantities such as luminosity and stellar mass. Since our lenses reside at relatively low redshifts we therefore have to correct our lens redshifts and derived quantities for this bias in order to achieve accurate object selection for our dark matter halo relations. Additionally, if this bias is not corrected for, the angular separations between lenses and sources will be altered, causing a coherent shift in the lensing signal radial binning. The resulting halo model fit will then also be affected, further illustrating the importance of this correction.

Following Hildebrandt et al. (2012), we perform our correction using spectroscopic redshifts in the overlap with the VI-

MOS VLT Deep Survey (VVDS; Le Fèvre et al. 2005; Garilli et al. 2008), the DEEP2 galaxy redshift survey (Davis et al. 2003, 2007; Newman et al. 2012) and the SDSS (Eisenstein et al. 2001; Strauss et al. 2002). The completeness of this spectroscopic sample is shown in Le Fèvre et al. (2005, Figure 16) and Newman et al. (2012, Figure 31). To ensure a completeness of at least 80%, we select only lenses with magnitude $i'_{AB} < 23$, as mentioned in Section 2.2. Since the bias is a function of magnitude and galaxy type, we start by splitting our sample in red and blue subsamples via their photometric type (as described in Section 2.1) and use several magnitude bins. We then quantify the bias in each bin by fitting a straight line of the form

$$(z_{\text{spec}} - 0.3) = a(z_{\text{phot}} - 0.3) + b \quad (\text{A1})$$

where z_{spec} is the spectroscopic redshift from VVDS/DEEP2/SDSS, z_{phot} is the CFHTLenS photometric redshift estimate, a is the slope and b is the offset. The pivot point of 0.3 roughly corresponds to the mean redshift of our lens sample, though the correction is insensitive to this number. The slope a is fit simultaneously in all magnitude bins but allowed different values for red and blue samples, while the offset b is allowed to vary between both type and magnitude bins. Keeping the slope fixed allows for a more robust estimate for the bias, though we have verified that allowing it to vary has negligible impact on the results in practice. The resulting fit parameters are shown in Table A1. Note that there is no correction performed for red galaxies beyond a magnitude of $i'_{AB} = 22$ since we do not use fainter red lenses (see Section 2.2).

We then use these fit parameters to correct our lens photometric redshift estimates in the range $0.2 \leq z \leq 0.4$. Calculating the luminosity distances and estimating the k-corrections corresponding to the original and corrected redshifts using the $g' - r'$ colours of the galaxies, we adjust the absolute magnitudes accordingly. We further derive new stellar mass estimates by scaling them to their new luminosities assuming a constant (pre-correction) stellar mass-to-luminosity ratio. The impact on the red galaxy properties is negligible, but for blue galaxies the correction is larger with the average luminosity and stellar mass increasing by $\sim 12\%$. We therefore proceed to use the corrected quantities in our luminosity and stellar mass analyses (see Sections 4 and 5).

The sources will also be affected by photometric redshift bias, but its impact on the measured halo masses is expected to be much smaller than the effect of the lens redshift bias. To confirm this hypothesis we shift all sources by a constant bias of 2% and redo the analysis of Sections 4 and 5. This bias value is most likely slightly larger than necessary (see Hildebrandt et al. 2012, Figure 4), but the resulting halo masses agree with the original halo masses within 1σ . We therefore do not need to correct our sources for photometric redshift bias.

A2 Photometric redshift scatter correction

Before interpreting the luminosity results we have to take into account the effect of Eddington bias (Eddington 1913). The precision of our photometric redshifts is high with a scatter of $\sigma_z \sim 0.04$ for both lenses and sources (Hildebrandt et al. 2012), but never the less the errors on the redshift estimates have to be taken into account. If the true redshift differs from the estimated one, this will affect all derived quantities. An underestimated redshift, for example, would cause the estimated absolute magnitude to be fainter than the true absolute magnitude and the lens would be placed in the wrong luminosity bin. As can be seen in Figure 4 there are more faint objects

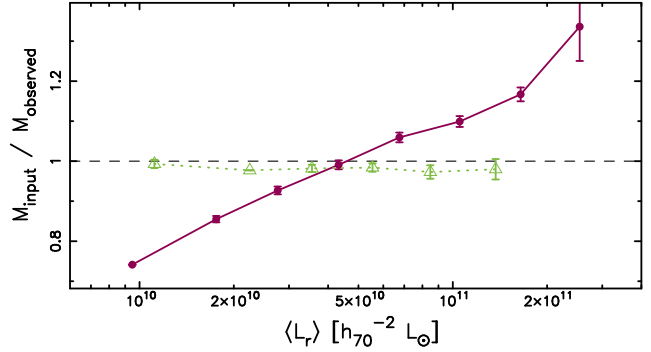


Figure A1. Correction factor as a function of luminosity induced through inaccuracies in the photometric redshift estimates. The dark purple solid (light green dotted) line with dots (triangles) shows the scatter correction factor for the red (blue) lens sample. The error bars show the scatter between 10 lens catalogue realisations.

Table A2. Photometric redshift scatter correction factors applied to observed halo masses in each luminosity bin (see Section 4) for red and blue lenses. These factors correct both for scatter due to redshift errors, and for the fact that the observed halo mass does not necessarily correspond to the mean halo mass.

Bin	$f_{\text{red}}^{\text{lscat}}$	$\sigma_{f,\text{red}}$	$f_{\text{blue}}^{\text{lscat}}$	$\sigma_{f,\text{blue}}$
L1	0.77	0.01	1.01	0.01
L2	0.88	0.01	1.00	0.00
L3	0.97	0.01	1.01	0.00
L4	1.05	0.01	1.02	0.01
L5	1.12	0.01	1.02	0.01
L6	1.19	0.02	1.03	0.02
L7	1.26	0.03	0.99	0.05
L8	1.40	0.07	0.00	0.00

than bright, which means that more objects will scatter from fainter bins into brighter bins than the other way around. This will lower the lensing signal in each bin and bias the observed halo mass low, and the amount of bias will be luminosity dependent. To estimate the impact of redshift scatter we create a simulated version of the CFHTLenS as follows. We fit an initial power law mass-luminosity relation of the form (see Equation 10, Section 4.1)

$$M_{200} = M_{0,L} \left(\frac{L}{L_{\text{fid}}} \right)^{\beta_L} \quad (\text{A2})$$

to the raw estimated halo masses, with $L_{\text{fid}} = 10^{11} h_{70}^{-2} L_{r',\odot}$. We then use this relation to assign halo masses to our lenses. Splitting the resulting lens catalogue in the usual magnitude bins for the red and blue sample separately we obtain our ‘true’ halo mass for each bin. Constructing NFW haloes from these halo masses at the photometric redshift of the lenses, we create mock source catalogues with the observed source redshift distribution but with simulated shear estimates with strengths corresponding to those which would be induced by our lens haloes. We then scatter the lenses and sources using the full redshift probability density function, split the lens catalogue according to the scattered magnitudes and measure the resulting signal within $200 h^{-1}$ kpc of the lenses using our scattered shear catalogue. We only use the small scales for our mass estimate to avoid complications due to insufficient treatment of clustering since on these scales only the central 1-halo signal is relevant, and we force our satellite fraction to zero to obtain a

pure NFW fit. This way we obtain the ‘observed’ halo mass for each magnitude bin. The ‘observed’ halo mass is then compared to the ‘true’ value for each bin. To increase the statistical precision of the correction we determine the average of 10 lens catalogue realisations. Since the starting point is a perfect signal, the number of realisations given the area is adequate to retrieve the correction factor. This correction simultaneously accounts for all the effects resulting from any photometric redshift scatter in our analysis, such as the scattering of lenses between luminosity bins, the effect on the lens and source redshift distributions, the smoothing of the signal due to mixing of the projected lens-source separations, and the non-linear dependence of the critical surface density Σ_{crit} on the lens and source redshifts. Note that the errors on the correction factors indicate only the propagated photometric redshift uncertainty, and even though they are small compared to the errors on the shear measurements, we have included them in our final error budget. The error on the correction factor does not include the uncertainties of the input parameters. However, we expect these additional uncertainties to be negligible compared to the errors on the halo masses (see the discussion in Appendix A3).

The results from this test are shown in Figure A1. The quality of our photometric redshifts is high which means that the correction factor is small overall, reaching only $\sim 30\%$ for a luminosity of $L_{r'} \sim 2.5 \times 10^{11} h_{70}^{-2} L_{\odot}$. Here the contamination is largest due to the shape of the luminosity function causing a larger fraction of low luminosity objects to scatter into the higher-luminosity bin. For our faintest red luminosity bin the correction is also $\sim 30\%$, in this case caused by larger errors in the photometric redshift estimates. The correction factor is less than unity for lower-luminosity bins due to the turn-over of the distribution of red lenses at $M_{r'} \sim -21.2$ (see Figure 4). The small correction factor for blue lenses is due to their flatter mass-luminosity relation (see Figure 6). Because of the relative insensitivity of halo mass to changes in luminosity, minor errors in luminosity measurements due to photometric redshift inaccuracies will not strongly affect the halo mass estimate. The process described in this appendix could in principle be iterated over, starting from the fitting of a mass-luminosity relation, until convergence is reached. Since Hoekstra et al. (2005) find that different choices for that relation yield similar curves, we choose not to iterate further.

We also have to correct our luminosity bins for a second scatter effect. As discussed in VU11 (Appendix B), the observed halo mass does not necessarily correspond to the mean halo mass in a given bin since the halo masses in that bin are not evenly distributed and the NFW profiles do not depend linearly on halo mass. The distribution within each bin generally follows a log-normal distribution, and to correct for this effect we follow a similar procedure as the one outlined in Appendix A3, with the difference that we do not scatter the luminosities as we have already corrected for that by accounting for the error in photometric redshift. We stress that this is an intrinsic effect unrelated to any measurement errors. The full correction factor, taking into account both scatter effects discussed here, is shown in Table A2.

The general procedure outlined in this appendix is repeated for the stellar mass bins, though we use the stellar mass-halo mass relation to assign halo masses to the mock lens catalogue, and then bin the lenses according to stellar mass rather than luminosity. In this case we do not use the resulting correction factor, but we do include the errors on said correction factor in our error budget in order to account for the above-mentioned effects in our stellar mass results. The correction factor itself, however, only conveys the impact of photometric redshift uncertainties, and not the additional

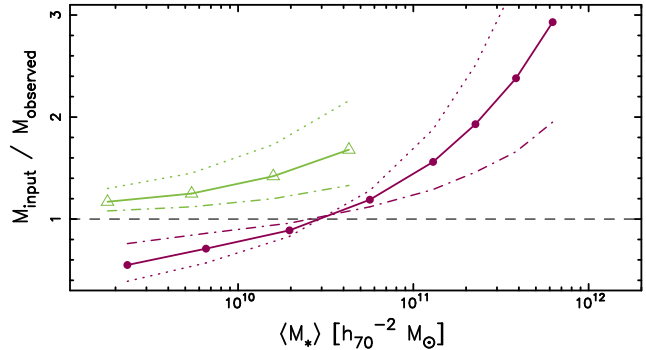


Figure A2. Mass correction factor as a function of stellar mass induced through inaccuracies in the stellar mass estimates. The dark purple solid dots (light green open triangles) show the correction factor for the red (blue) lens sample. As discussed in the text, the dot-dashed lines show the correction factors if stellar mass errors of 0.2 dex are assumed, rather than the default 0.3 dex, and the dotted lines show the correction factors derived using stellar mass errors of 0.4 dex.

Table A3. Bin scatter correction factors applied to observed halo masses in each stellar mass bin (see Section 5) for red and blue lenses. These factors correct both for scatter due to stellar mass errors, and for the fact that the observed halo mass does not necessarily correspond to the mean halo mass.

Bin	$f_{\text{red}}^{\text{mscat}}$	$f_{\text{blue}}^{\text{mscat}}$
S1	0.55	1.17
S2	0.71	1.25
S3	0.89	1.42
S4	1.19	1.68
S5	1.56	—
S6	1.93	—
S7	2.38	—
S8	2.93	—

effects influencing the stellar mass errors. The scatter due to stellar mass errors is accounted for following the method described in the next appendix, and applying this correction factor as well would therefore amount to double-counting.

A3 Stellar mass bin scatter correction

In a process similar to the scatter in luminosity, objects will scatter between stellar mass bins due to errors on the stellar mass estimates. Though objects scatter randomly according to their individual stellar mass errors, the net effect will be to scatter lenses from greater abundance to lower according to the stellar mass function (SMF). Because the stellar mass function declines steeply at higher stellar mass bins, these will be more severely affected by low-mass object contamination. As a result the observed lensing mass in the highest stellar mass bins will be biased low (see Appendix A in VU11). Additionally, the lensing halo mass estimates will be affected by the fact that the observed halo mass does not necessarily correspond to the mean halo mass in a given bin, as discussed in Appendix A2.

To assess the impact of both these effects simultaneously we follow a procedure similar to the one used to correct for redshift scatter, as described in the previous appendix. We start by fitting an initial power law halo mass-stellar mass relation using the raw observed lensing halo mass. Drawing a large number of simulated

lens galaxies from the stellar mass function, we take these stellar masses to be the true unscattered values and assign a halo mass according to the fitted halo mass-stellar mass relation. As described above, this halo mass will be distributed within the stellar mass bin according to some distribution. Following VU11 we therefore correct the halo mass for this effect by drawing from a log-normal distribution with a mean given by the original halo mass and a width determined by More et al. (2011). We now know the ‘true’ mean halo mass for each bin. Using the resulting simulated lens catalogue we create a source catalogue with shears determined analytically. We then scatter the lenses assuming a Gaussian error distribution with a width of 0.3 dex as appropriate for our stellar mass errors (see Section 2.1) to create a new simulated lens catalogue, this time containing ‘observed’ stellar masses. Dividing this ‘observed’ lens catalogue according to the usual stellar mass bins for red and blue samples separately, we measure the signal in the simulated shear catalogues and again fit an NFW profile. This way we obtain the ‘observed’ halo mass for each stellar mass bin. By taking the ratio of simulated ‘observed’ to ‘true’ halo mass we arrive at the correction factor for stellar mass scatter as shown in Figure A2. We can now apply this factor, as quoted in Table A3, to our halo mass estimates to correct for the scatter between stellar mass bins, and for the fact that the observed halo mass does not correspond to the mean halo mass, simultaneously.

The correction factor is relatively sensitive to the adopted value of the stellar mass error, particularly in the regime where the stellar mass function is steep. Therefore, in addition to the correction factor used, we also show in Figure A2 the correction factors obtained if we adopt a stellar mass error of 0.2 dex or 0.4 dex instead, covering the plausible range of values that the stellar mass error could take. This illustrates how the correction factor coherently shifts if the stellar mass error is different from what we assume. For S8 of the red lenses, the change is largest, with an increase (decrease) of the correction factor by $\sim 50\%$ for 0.4 dex (0.2 dex), respectively. We do not use the plausible range of correction factors as the error on the correction, since a different stellar mass error would only lead to a coherent shift of all the correction factors and hence of the corrected halo masses. This property of the correction factors would be lost, and the error bars on the halo masses would be severely overestimated, causing an unjustified loss of information. However, for completeness, we note that the best fit power law normalisation and slope are $1.00 \pm 0.05 \times 10^{13} h_{70}^{-1} M_{\odot}$ ($0.66^{+0.10}_{-0.11} \times 10^{13} h_{70}^{-1} M_{\odot}$) and 1.35 ± 0.05 ($0.78^{+0.05}_{-0.04}$) for red (blue) lenses when we adopt a stellar mass error of 0.2 dex, and $1.63^{+0.08}_{-0.11} \times 10^{13} h_{70}^{-1} M_{\odot}$ ($1.17 \pm 0.18 \times 10^{13} h_{70}^{-1} M_{\odot}$) and $1.61^{+0.06}_{-0.04}$ ($0.87^{+0.05}_{-0.04}$) for red (blue) lenses for a stellar mass error of 0.4 dex.

Additionally, the correction factor has some error due to the uncertainties of the other input parameters, such as in the adopted power law relations, the stellar mass functions, and the scatter in halo mass. VU11 found that the correction is fairly insensitive to changes in the power law relation; using the power law obtained *after* the stellar mass scatter correction only changed the correction factor by at most 4%. The impact here will be even smaller as the power laws are less steep, and we therefore ignore their effect. Next, the stellar mass function is not the intrinsic stellar mass function as objects have already scattered. However, we cannot reliably obtain the intrinsic stellar mass function where it matters most, i.e. at the high stellar mass range, as the number of galaxies is too low. We therefore do not attempt to obtain the intrinsic stellar mass function, but rather note this as a caveat. Finally, we note that the

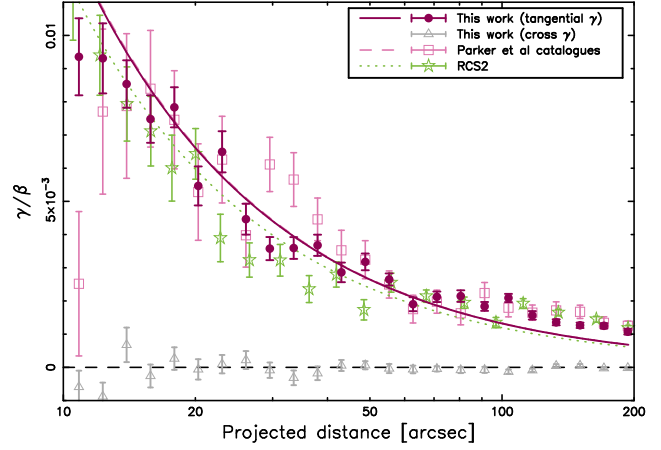


Figure B1. Comparison of three data sets: the shear catalogues from $\sim 22 \text{ deg}^2$ CFHTLS (pink open squares), the results from RCS2 (light green open stars) and our results (dark purple solid dots). The curves show the best-fit singular isothermal sphere for each dataset (with light green and pink nearly identical), and the grey triangles show the cross-shear from our results which should be zero in the absence of systematic errors.

correction factor is insensitive to the adopted width of the halo mass distribution.

APPENDIX B: TESTS FOR GALAXY-GALAXY LENSING SYSTEMATICS

B1 Initial consistency analysis of the CFHTLenS catalogue

In this study we use lenses and sources from the full 154 deg^2 CFHTLenS catalogue. The accuracy of the CFHTLenS shears has been verified through several rigorous tests aimed at the study of cosmic shear (Heymans et al. 2012; Miller et al. 2013), but it is interesting to compare the galaxy-galaxy lensing signal with the results from two previous analyses of a similar nature. The first is the galaxy-galaxy lensing analysis in the CFHTLS-Wide conducted by Parker et al. (2007), and the second is based on the shear catalogue from VU11 (see Section 6). In Parker et al. (2007) an area of $\sim 22 \text{ deg}^2$ in i' was analysed, corresponding to about 14% of our area. Since they only had data from one band their analysis also lacked redshift estimates for lenses and sources, but they separated lenses from sources using magnitude cuts. The shear estimates for their sources were obtained using a version of the technique introduced by Kaiser, Squires, & Broadhurst (1995) as outlined in Hoekstra et al. (1998). These shear estimates were measured on a stacked image rather than obtained by fitting all exposures simultaneously (see Miller et al. 2013, for a discussion on this). To avoid the strong PSF effects at the chip boundaries, Parker et al. (2007) limited their analysis to the unique chip overlaps. In contrast we are able to use all the data we have at our disposal. The data from VU11 is the subset of ~ 400 square degrees of the RCS2 with i' -band coverage, which is shallower than the CFHTLS and for which also no redshifts were available for the sources at the time of this analysis.

To compare and contrast our lensing signal with these previous works we mimic the analysis presented in Parker et al. (2007) as closely as possible and apply the same i' -band magnitude cuts as employed in Parker et al. (2007), with $19.0 < i'_{AB} < 22.0$ for lenses and $22.5 < i'_{AB} < 24.5$ for sources. Parker et al. (2007) boost their signal to correct for contamination by sources that are

physically associated with the lens, and we apply the same correction factor to our values. The resulting galaxy-galaxy signal, scaled with the angular diameter distance ratio $\langle\beta\rangle = \langle D_{ls}/D_s \rangle = 0.49$ from Parker et al. (2007), is shown as dark purple solid dots in Figure B1. We also re-analysed the original shear catalogues used for the Parker et al. (2007) analysis with the results shown as pink open squares in Figure B1. The signal from the VU11 shape measurement catalogues of the RCS2 is obtained using a source selection of $22 < r' < 24$ instead because the limiting depth in i' is 23.8 for the RCS2. The measurements are also corrected for contamination by physically associated sources, as described in VU11, and scaled with $\langle\beta\rangle = 0.30$ which is determined by integrating over the lens and source redshift distributions that were obtained from the CFHTLS “Deep Survey” fields (Ilbert et al. 2006). The measurements are shown as light green open stars. Figure B1 shows that the lensing signals generally agree well. We fit an SIS profile to the shear measurements that have been scaled by $\langle\beta\rangle$ on scales between 7 and 120 arcsec, and find a scaled Einstein radius of $\tilde{r}_E = 0.277 \pm 0.006$ arcsec for our results, $\tilde{r}_E = 0.267 \pm 0.011$ arcsec for the Parker et al. (2007) measurements and $\tilde{r}_E = 0.262 \pm 0.007$ arcsec for VU11, which are broadly consistent.

The best-fit SIS profile corresponds to a velocity dispersion of $\sigma_v = 97.9 \pm 1.0 \text{ km s}^{-1}$, which is lower than the $\sigma_v = 132 \pm 10 \text{ km s}^{-1}$ quoted in Parker et al. (2007). However, using the re-analysed Parker et al. (2007) shear catalogue we find a velocity dispersion of $\sigma_v = 96.6 \pm 2.0 \text{ km s}^{-1}$. For the VU11 results we find a velocity dispersion of $\sigma_v = 95.4 \pm 1.3 \text{ km s}^{-1}$, slightly lower but in reasonable agreement with our results. Note that there are various small differences between the analyses, such as different effective source redshift distributions and different weights applied to the shears. Additionally we use the multiplicative bias correction factor for our measurements, while the other works did not have such a correction. All these differences could have small but non-negligible effects on the results. The discrepancy with the velocity dispersion quoted in Parker et al. (2007) remains unexplained, but we conclude that the shear estimates are in fact fully consistent.

B2 Seeing test

Miller et al. (2013) isolated a general multiplicative calibration factor as a function of the signal-to-noise ratio and size of the source galaxy, $m(\nu_{SN}, r)$, using simulations. To confirm the successful calibration of the CFHTLenS shears in the context of galaxy-galaxy lensing, we study how a shear bias relates to image quality. In general a round PSF causes circularisation of source images which in turn can cause a multiplicative bias of the measured shapes if it is not properly corrected for. Such a systematic would depend on the size of the PSF. Assuming that the systematic offset due to PSF anisotropy is negligible (a fair assumption given our correction for spurious signal around random lenses; see Section 3.1 and the detailed analysis of PSF residual errors in Heymans et al. (2012)), and assuming that the shapes of very well resolved galaxies can be accurately recovered, the observed average shear in a galaxy-galaxy lensing azimuthal distance bin is related to the true average shear via

$$\langle\gamma^{\text{obs}}\rangle = \langle\gamma^{\text{true}}\rangle \left[1 + \mathcal{M} \left\langle \left(\frac{r_*}{r_0} \right)^2 \right\rangle \right]. \quad (\text{B1})$$

where γ^{obs} is the observed shear, γ^{true} is the true shear, r_* is the PSF size, r_0 is the intrinsic (Gaussian) size of the galaxy and \mathcal{M} is a value close to zero representing the multiplicative bias. The

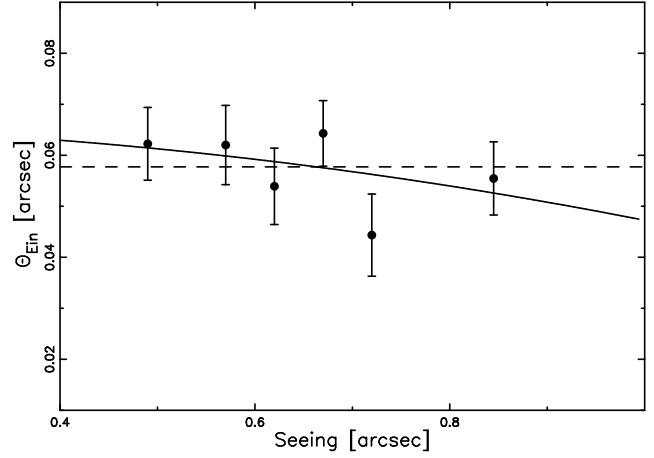


Figure B2. Galaxy-galaxy lensing signal quantified through the best-fit Einstein radius (see Equation B2) as measured in each of 6 seeing bins, according to Table B1. The solid line shows the best-fit model using Equation B3 while the dashed line shows the average Einstein radius assuming no bias.

Table B1. Details of the seeing bins.

Sample	N_{fields}	$\langle r_* \rangle$ [arcsec]	θ_E [arcsec]	σ_{θ_E}
P1	27	0.50	0.053	0.005
P2	23	0.57	0.044	0.006
P3	33	0.62	0.050	0.005
P4	38	0.67	0.047	0.005
P5	28	0.72	0.040	0.006
P6	36	0.80	0.049	0.005

particular dependence on PSF size is the result of a full moments analysis (see for example Paulin-Henriksson et al. 2008).

Since the bias depends on the size of the PSF relative to the size of galaxies, data with a spread in seeing should enable us to determine the bias \mathcal{M} directly from the data, thus allowing us to deduce the true performance of the shape measurement pipeline. The CFHTLS images have such a spread, with the best seeing being 0.44 arcsec and the worst being 0.94 arcsec, and therefore provides us with a neat way of determining this bias. Since at small projected separations from the lens, the tangential shear signal is generally well described by an SIS profile:

$$\gamma(\theta) = \frac{\theta_E}{2\theta} \quad (\text{B2})$$

where θ is the distance to the lens and θ_E is the Einstein radius, we therefore have a simple relationship between the observed Einstein radius and the true one:

$$\theta_E^{\text{obs}} = \theta_E^{\text{true}} \left[1 + \mathcal{M} \left\langle \left(\frac{r_*}{r_0} \right)^2 \right\rangle \right]. \quad (\text{B3})$$

By measuring the Einstein radius of the average lens as a function of seeing we can therefore determine both the true Einstein radius and the performance of the shape measurement pipeline.

We select our lenses in magnitude and redshift as described in the main paper (Section 2.2), though we do not distinguish between red and blue galaxies, and we also split our data according to Table B1. Dividing the data according to image quality in this way may imply some minor selection effects, such as redshift and magnitude estimates being less accurate for worse seeing and thus

PSF. Since great care has been taken to correct for such effects (see Hildebrandt et al. 2012) we will assume here that the lens samples are comparable between seeing bins. Having selected our lenses, we measure the galaxy-galaxy lensing signal in each seeing bin and fit an SIS to the innermost $200 h_{70}^{-1}$ kpc. By fitting only small scales we avoid the influence of neighbouring haloes. The results are shown in Figure B2 and quoted in Table B1. We then fit the relation described by Equation B3 to the resulting Einstein radii and find a value of $\mathcal{M} = -0.071 \pm 0.075$. This is consistent with no bias, a fact which is further illustrated in Figure B2; the data points agree with an average Einstein radius of 0.058 ± 0.003 , shown as a dashed line.

APPENDIX C: DETAILED LUMINOSITY BINS

In this Appendix we show the decomposition of the best-fit halo model for red (Figure C1) and blue (Figure C2) lenses, split in luminosity according to Table 1. Showing the full decomposition is highly informative because it highlights some of the major trends and clarifies which effects dominate in each case.

The baryonic component based on the mean stellar mass in each bin (dark purple dot-dashed line) becomes more dominant for higher luminosities, but the luminous size of the lenses also increases, making measurement of background source shapes in the innermost distance bins difficult. Thus it is not possible to reliably constrain the baryonic component with our data. Yet the effect of including the baryons in our model is an overall lowering of the dark matter halo profile (dark purple dashed) compared to the model without baryons. For the red lenses we see that a considerable fraction of the sample at lower luminosities necessarily consists of satellite galaxies, since there is a clear bump in the signal at intermediate scales which has to be accounted for. This satellite fraction continuously drops as luminosity increases, and simultaneously becomes more difficult to constrain since the combination of the stripped satellite profile (light green dash-dotted) and satellite 1-halo terms (light green dashed) becomes almost indistinguishable from a single NFW profile for high halo masses. This effect was discussed in more detail in VU11, Appendix C.

For the blue lenses, the signal becomes very noisy for the two highest-luminosity bins due to a lack of lenses. These two bins are therefore discarded from the full analysis in Section 4. In general, blue galaxies produce a noisier signal than red galaxies for the same luminosity cuts. This could be because blue lenses are in general less massive, and there are fewer of them which results in a weaker signal and a lower signal-to-noise for most bins. It could also be an indicator that the physical correlation between stellar mass and halo mass is noisier for these lenses. We also notice that nearly all blue lenses are galaxies located at the centre of their halo, rather than being satellites. This is consistent with previous findings. It is possible that satellite galaxies in general are redder because they have been stripped of their gas and thus have had their star formation quenched. It could also mean that most blue galaxies in our analysis are isolated; we have made no distinction between field galaxies and galaxies in a more clustered environment. If blue galaxies are more isolated than red ones then the contribution from nearby haloes (dotted lines) would also be less. It is clear from Figure C2 that the large scales are not optimally fit by our model, and isolation may be one of the reasons since we assume the same mass-bias relation for blue galaxies as for red. With current data it is not possible to constrain the bias as a free parameter, but with future wider surveys this could be done.

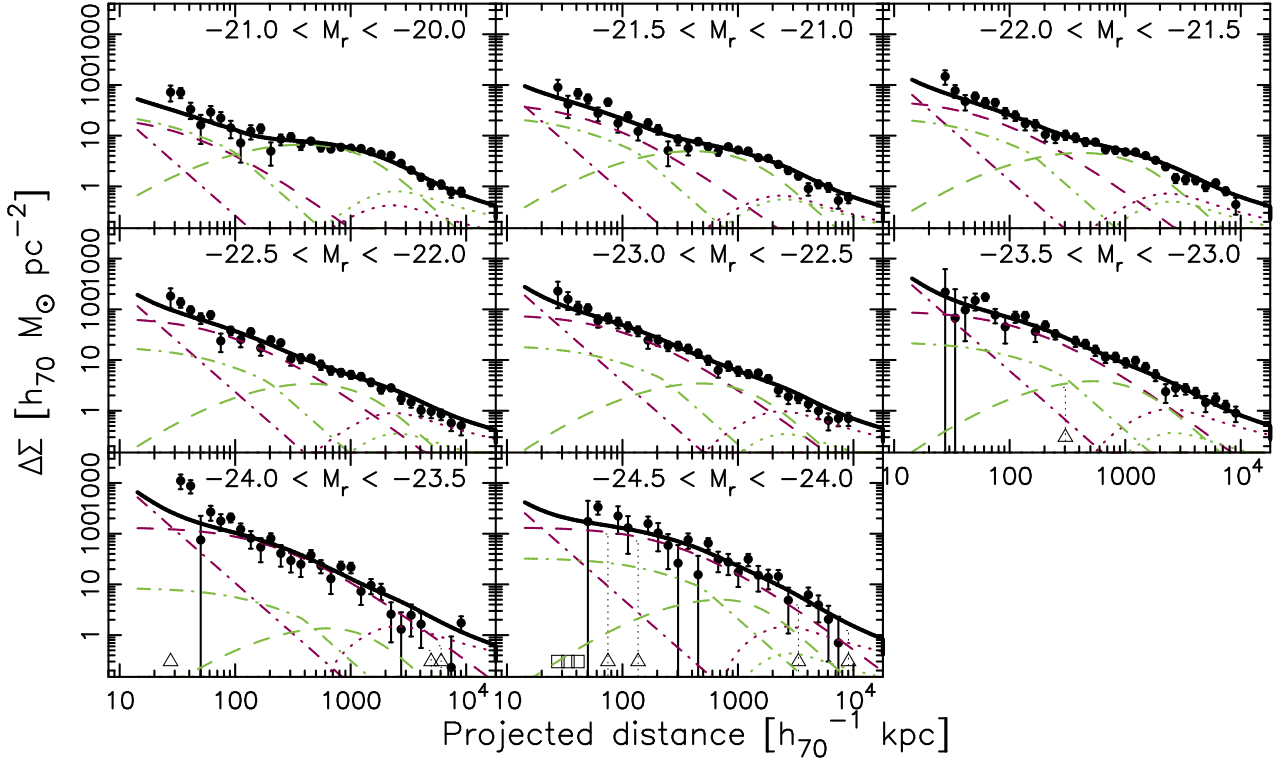


Figure C1. Galaxy-galaxy lensing signal around *red* lenses which have been split into luminosity bins according to Table 1, and modelled using the halo model described in Section 3.2. The black dots are the measured differential surface density, $\Delta\Sigma$, and the black line is the best-fit halo model with the separate components displayed using the same convention as in Figure 3. Grey triangles represent negative points that are included unaltered in the model fitting procedure, but that have here been moved up to positive values as a reference. The dotted error bars are the unaltered error bars belonging to the negative points. The grey squares represent distance bins containing no objects.

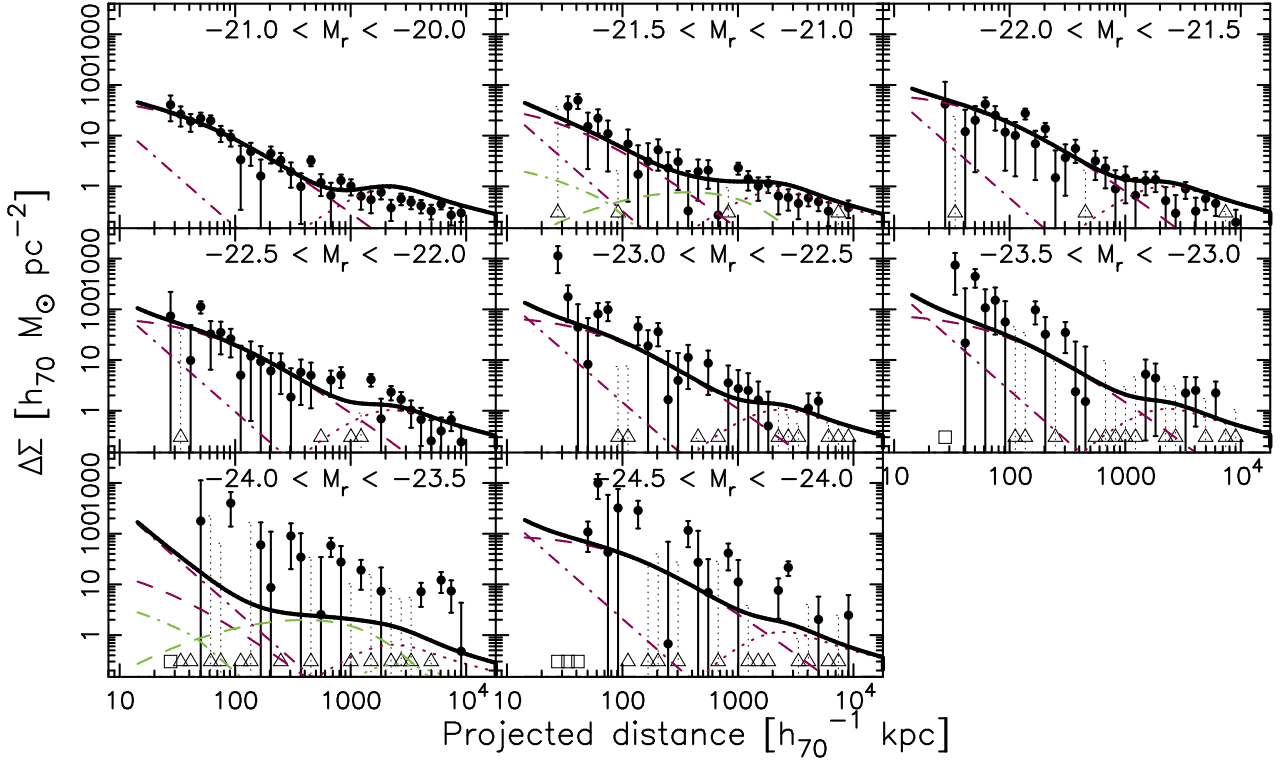


Figure C2. Galaxy-galaxy lensing signal around *blue* lenses which have been split into luminosity bins according to Table 1, and modelled using the halo model described in Section 3.2. The black dots are the measured differential surface density, $\Delta\Sigma$, and the black line is the best-fit halo model with the separate components displayed using the same convention as in Figure 3. Grey triangles represent negative points that are included unaltered in the model fitting procedure, but that have here been moved up to positive values as a reference. The dotted error bars are the unaltered error bars belonging to the negative points. The grey squares represent distance bins containing no objects.

APPENDIX D: DETAILED STELLAR MASS BINS

The decomposition of the best-fit halo model for red and blue lenses, divided using stellar mass as detailed in Table 3, is shown in Figures D1 and D2 respectively.

By construction the baryonic component amplitude (dark purple dash-dotted line) increases with increasing bin number, and so does the dark matter halo mass (dashed lines). Note that with our stellar mass selections we push to smaller and fainter objects, so the objects in the three lowest-mass bins are on average less massive and less luminous than the galaxies in the faintest luminosity bin. In these bins, nearly all red galaxies are satellites, while for higher stellar mass bins the satellite fraction diminishes, a behaviour which is consistent with the trends we saw for luminosity (Appendix C). For the higher stellar mass bins, as for the higher luminosity bins, the sum of the satellite stripped and 1-halo terms result in a profile which resembles a single NFW profile, making the satellite fraction more difficult to determine. For the blue lenses we run into the same issues for the highest mass bin as for the highest luminosity bins; the number of lenses is too small to constrain the halo model and so the bin has to be discarded. Furthermore, the satellite fraction is low across all blue lens bins indicating that these lenses are most likely isolated, which is consistent with the low large-scale signal and with our findings for luminosity.

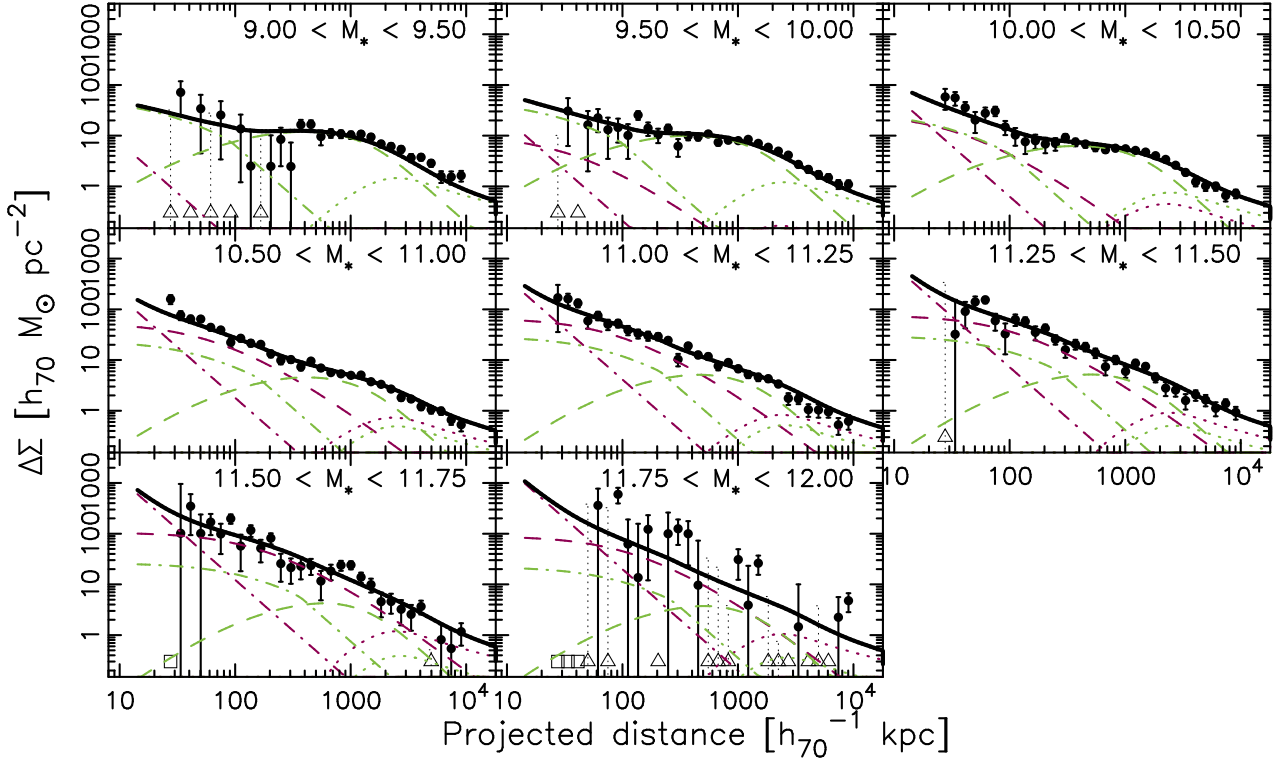


Figure D1. Galaxy-galaxy lensing signal around *red* lenses which have been split into stellar mass bins according to Table 3, and modelled using the halo model described in Section 3.2. The black dots are the measured differential surface density, $\Delta\Sigma$, and the black line is the best-fit halo model with the separate components displayed using the same convention as in Figure 3. Grey triangles represent negative points that are included unaltered in the model fitting procedure, but that have here been moved up to positive values as a reference. The dotted error bars are the unaltered error bars belonging to the negative points. The grey squares represent distance bins containing no objects.

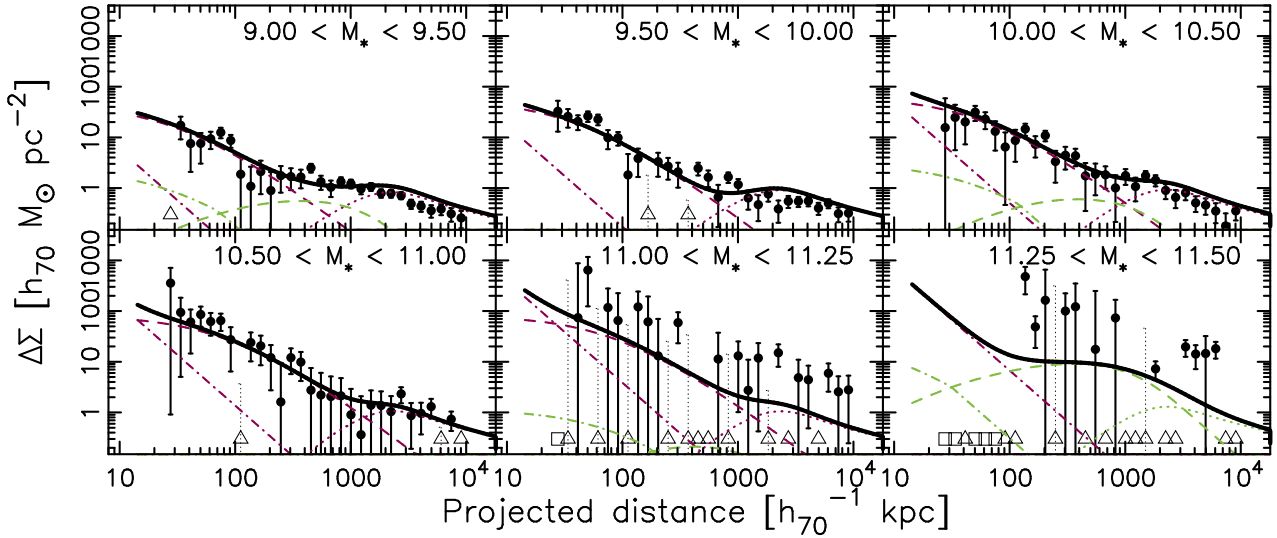


Figure D2. Galaxy-galaxy lensing signal around *blue* lenses which have been split into stellar mass bins according to Table 3, and modelled using the halo model described in Section 3.2. The black dots are the measured differential surface density, $\Delta\Sigma$, and the black line is the best-fit halo model with the separate components displayed using the same convention as in Figure 3. Grey triangles represent negative points that are included unaltered in the model fitting procedure, but that have here been moved up to positive values as a reference. The dotted error bars are the unaltered error bars belonging to the negative points. The grey squares represent distance bins containing no objects.